

Sources of ore–forming fluids and Co metal in the Xiji hydrothermal Cu–Co deposit, West Qinling Orogen: Constraints from S–Sr isotopes

Pan–fei Sun, Zhao Liu, Yong–sheng Li, Hai–rui Sun, Xue–feng Li, Shi–min Zhen, Jin–chi Xu, Shi–xu Zhou, Yong–qiang Liu, Qing–fei Wang

Citation: Pan–fei Sun, Zhao Liu, Yong–sheng Li, Hai–rui Sun, Xue–feng Li, Shi–min Zhen, Jin–chi Xu, Shi–xu Zhou, Yong–qiang Liu, Qing–fei Wang, 2025. Sources of ore–forming fluids and Co metal in the Xiji hydrothermal Cu–Co deposit, West Qinling Orogen: Constraints from S–Sr isotopes, China Geology, 8, 1–22. doi: 10.31035/cg2025132.

View online: http://www.jos.ac.cn/article/shaid/8937ff461e408b5a65ee43d71d28c18a7260cfc6d074faa77622440d48f3f974

Related articles that may interest you

Mineralization of the Liwu large–scale stratiform copper deposits in Sichuan Province, China: Constraints from fluid inclusions
China Geology. 2023, 6(2), 252 https://doi.org/10.31035/cg2023034

Geology, mineralization and model of the giant Maoping carbonate–hosted Pb–Zn deposit (5 Mt), South China
China Geology. 2025, 8(2), 431 https://doi.org/10.31035/cg2024142

Geology, geochronology, and exploration of the Jiama giant porphyry copper deposit (11 Mt), Xizang, China: A review
China Geology. 2023, 6(2), 338 https://doi.org/10.31035/cg2023031

Geology and mineralization of the Sanshandao supergiant gold deposit (1200 t) in the Jiaodong Peninsula, China: A review
China Geology. 2021, 4(4), 686 https://doi.org/10.31035/cg2021070

Melt extraction and mineralization: A case study from the Shuangjianzishan supergiant Ag–Pb–Zn deposit (208 Mt), Inner Mongolia, NE China
China Geology. 2023, 6(4), 623 https://doi.org/10.31035/cg2022044

The copper polymetallic deposits and resource potential in the Xizang Plateau
China Geology. 2021, 4(1), 1 https://doi.org/10.31035/cg2021016

China Geology 8 (2025) 1−22

China Geology

Journal homepage: http://chinageology.cgs.cn
https://www.sciencedirect.com/journal/china-geology

Sources of ore-forming fluids and Co metal in the Xiji hydrothermal Cu-Co deposit, West Qinling Orogen: Constraints from S-Sr isotopes

Pan-fei Sun[a, b, c,1], Zhao Liu[d,1], Yong-sheng Li[a, b,*], Hai-rui Sun[a, b], Xue-feng Li[a, b], Shi-min Zhen[a, b], Jin-chi Xu[a, b], Shi-xu Zhou[a, b], Yong-qiang Liu[a, b, e], Qing-fei Wang[c, d]

[a] *Development and Research Center, China Geological Survey, Ministry of Natural Resources, Beijing* 00037, *China*
[b] *Mineral Exploration Technical Guidance Center, Ministry of Natural Resources of the People's Republic of China, Beijing* 100037, *China*
[c] *State Key Laboratory of Geological Processes and Mineral Resources, China University of Geosciences (Beijing), Beijing* 100083, *China*
[d] *Jiangxi Provincial Key Laboratory of Genesis and Prospect for Strategic Minerals, East China University of Technology, Nanchang* 330013, *China*
[e] *College of Earth Science, Chengdu University of Technology, Chengdu* 610059, *China*

ARTICLE INFO

Article history:
Received 3 June 2025
Received in revised form 29 October 2025
Accepted 30 October 2025
Available online 27 November 2025

Keywords:
Hydrothermal Co deposit
Ore-forming fluid source
Metal source
S-Sr isotopes
Genetic model
Mineral exploration engineering
West Qinling Orogen

ABSTRACT

Economically significant hydrothermal Co deposits are a distinct deposit type. However, the sources of ore-forming fluids and Co metal are poorly constrained. This study addresses this issue using mineral paragenesis, geochemistry, and *in situ* S and Sr isotope data from the Xiji Cu-Co deposit of the West Qinling Orogen. Co mineralization associated with cobaltite, pyrite, calcite, and sericite assemblages is controlled by the bends of brittle-ductile shear zones in the Devonian strata. The $\delta^{34}S$ values of chalcopyrite and pyrites in the Cu and Co mineralization stages are +6.19‰ to +10.16‰ and +5.69‰ to +12.03‰, respectively, and the $^{87}Sr/^{86}Sr$ ratio of calcite ranges from 0.709347 to 0.711368, suggesting that ore-forming fluids were derived from the Neoproterozoic metamorphic basement analogous to the Bikou Group. The numerous meta-mafic rocks in the metamorphic basement, the increasing $^{87}Sr/^{86}Sr$ ratio in four calcite stages, and the inconsistency in pyrite $\delta^{34}S$ values of two mafic dikes imply that Co was predominantly sourced from the metamorphic basement, with the preexisting mafic dike providing a minor contribution. The similarity in $\delta^{34}S$ values between the Xiji and Dengjiagou deposits strengthens the interpretation. Accordingly, this study proposes a novel ore-forming model in which the metamorphic basement supplies ore-forming fluids and Co metal for hydrothermal Co mineralization systems. The findings confirm the significant Co exploration potential in the study area.

©2025 China Geology Editorial Office.

1. Introduction

The strategic importance of cobalt has become increasingly recognized due to the rapid development of new energy industries (Wang Y et al., 2021). Co deposits can be classified into four genetic types: Sedimentary-metasedimentary, magmatic, hydrothermal, and weathered laterite deposits (Zhao JX et al., 2019; Zhang HR et al., 2020; Chen C et al., 2024). Hydrothermal Co deposits represent the most economically significant type, accounting for 49% of the proven cobalt resources in the continental crust and 62% of global production (Zhang HR et al., 2020). Such Co deposits are widely distributed globally and include Katanga and Mutanda in the Central African Copperbelt (Cailteux JLH et al., 2005; Saintilan NJ et al., 2018; Sośnicka M et al., 2019), Blackbird in the United States (Slack JF et al., 2010), and Bou Azzer in Morocco (Wafik A et al., 2024; Saintilan NJ et al., 2023). However, the formation of hydrothermal cobalt deposits in the Earth's crust remains unclear (McGowan RR et al., 2006; El Desouky HA et al., 2009; Sośnicka M et al., 2019; Zhang LC et al., 2023).

The mechanisms of cobalt transport and precipitation are well understood. Cobalt in hydrothermal environments predominantly migrates as n-divalent chlorine complexes (Wood SA et al., 2007; Liu WH et al., 2011). The fluid's temperature and salinity significantly affect cobalt solubility.

First author: *E-mail address*: sunpanfei1994@126.com (Pan-fei Sun); liuzhao@ecut.edu.cn (Zhao Liu).

* Corresponding author: *E-mail address*: Liysh1983@126.com (Yong-sheng Li).

1 This author should be considered joint first author.

Literary editor: Li-qiong Jia
doi:10.31035/cg2025132
2096-5192/© 2025 China Geology Editorial Office.

Cooling and dilution of the fluid decrease the solubility of cobalt and the stability of $CoCl_4^{2-}$ in the hydrothermal solution, leading to the precipitation of cobalt metal (Liu W et al., 2011). However, the sources of Co metals and ore-forming fluids in hydrothermal Co deposits remain poorly constrained. Co abundance is the highest in the Earth's core and mantle (Su BX et al., 2023). Mafic magmatic activity facilitates cobalt mobilization and subsequent distribution in the Earth's reservoirs (Sillitoe RH et al., 2017). Consequently, mafic rocks (Holzheid A et al., 1996; Van Wilderode J et al., 2015), the metamorphic basement (McGowan RR et al., 2006; Sillitoe RH et al., 2015; Sillitoe RH et al., 2017), and sedimentary formations (Brown AC, 2014; Qiu ZJ et al., 2021) have been proposed as potential sources of Co metals. Research on Co deposits has characterized various ore-forming fluids, with basin fluids (McGowan RR et al., 2006; El Desouky HA et al., 2009; Saintilan NG et al., 2018; Sośnicka M et al., 2019), magmatic hydrothermal fluids (Bending JS et al., 2001; Johnson CA et al., 2012), and metamorphic hydrothermal fluids (Tian F et al., 2017; Lu YG et al., 2021; Qiu ZJ et al., 2021; Wang HN et al., 2023) being the most widely recognized. Accurately characterizing the sources of ore-forming fluids and Co metals is critical for understanding the formation of hydrothermal cobalt deposits.

The West Qinling Orogen experienced the breakup of the Neoproterozoic Rodinian supercontinent and the convergence of the East Asian continent (Feng YM et al., 2003; Zhang GW et al., 1995; Dong YP et al., 2016; Guo MX et al., 2024). Its tectonic background is similar to that of the Central African Copperbelt, the world's largest cobalt metallogenic belt. Both have extensive meta-mafic rocks in the ancient metamorphic basement, which is considered cobalt-rich (Large RR et al., 2019; Sillitoe RH et al., 2017). Recent explorations have revealed numerous Co deposits and mineralization indicators predominantly in Devonian sequences, Silurian sequences, and Neoproterozoic metamorphic basement terranes (Fig. 1). Co mineralization occurs frequently and is spatially and genetically associated with Cu, Mn, and Au mineralization. The discovery of Co hotspots in the region has validated the potential for Co mineralization, rendering it an ideal study area (Duan XP et al., 2024).

The Xiji Cu-Co deposit occurs in a mineral district with several other hydrothermal Co deposits under exploration, including the Shangtong and Dengjiagou Cu-Co deposits, which have similar structural frameworks. The Xiji deposit represents the most thoroughly explored site, where copper mining operations have begun. It exhibits the most advanced cobalt mineralization, with significant amounts of erythrite on

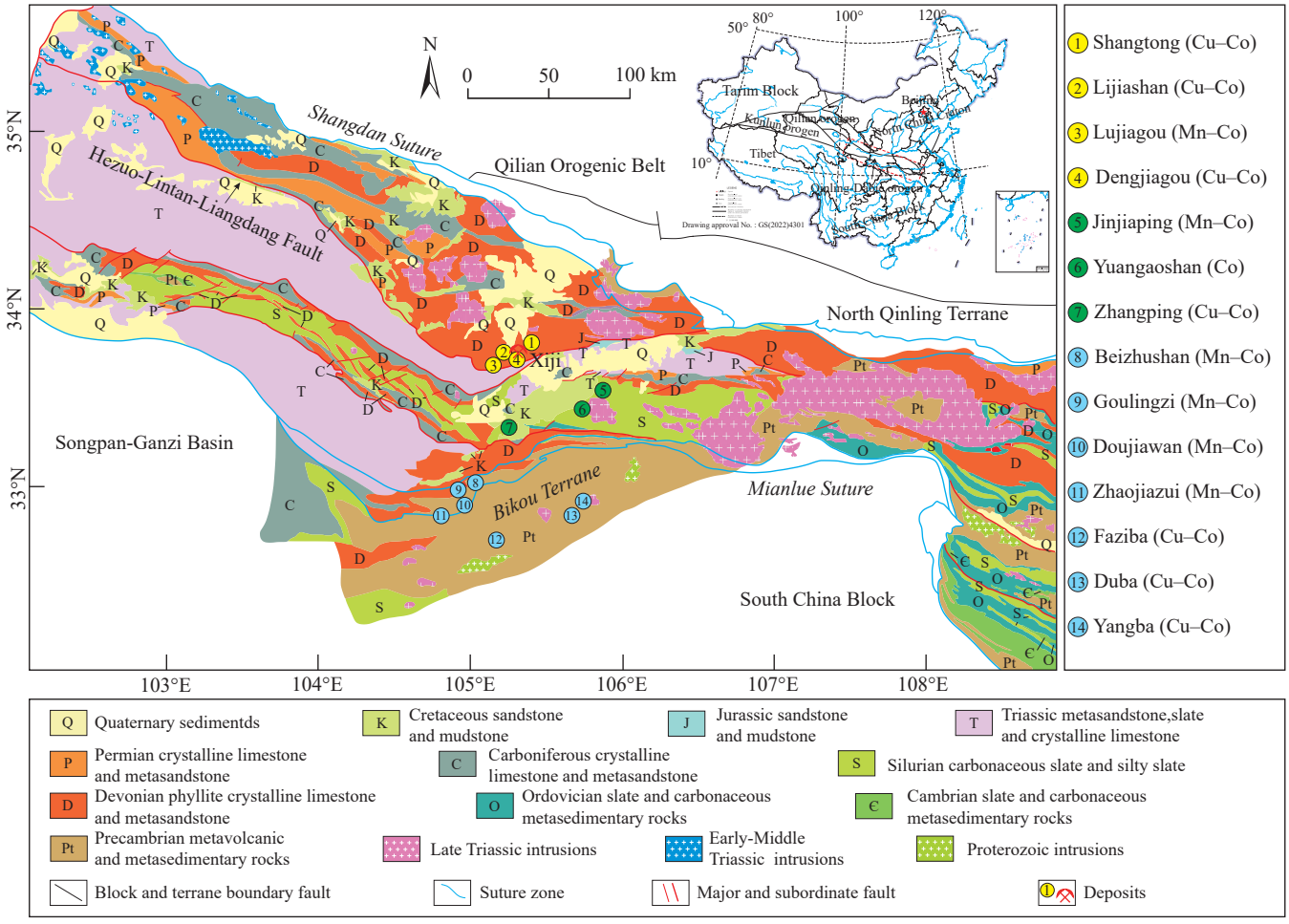


Fig. 1. Geological map of the West Qinling Orogen, showing main rock units, structures, and distribution of Cu-Co, Mn-Co, Co deposits (modified from Wu GL et al., 2014; Liu JJ et al., 2015; Yan Z et al., 2016; Zhao HS et al., 2021). Inset map indicates tectonic location of the geological map.

slate surfaces in adits and Co grades of 0.1×10^{-2}, demonstrating considerable potential for economic Co mineralization. The deposit is regarded as a representative Co deposit. Therefore, this study selected it to investigate the sources of ore-forming fluids and Co metal and elucidate the genetic model of Co deposits in the West Qinling Orogen. The structural geometry, crosscutting relationships, and mineral assemblages were examined using electron probe microanalysis of pyrite, S isotope analysis of pyrite and chalcopyrite, and Sr isotope analysis of calcite via laser ablation-inductively coupled plasma-mass spectrometry (LA-ICP-MS).

2. Geological setting

The West Qinling Orogen is part of the Qinling-Dabie Orogenic Belt located between the North China Craton and the South China Block (Fig. 1). The West Qinling Orogen is bound by the Shangdan suture to the north and by the Mianlue suture to the south and is located at the convergence of the Qinling-Qilian-Kunlun orogenic belt (Ren J, 1996). The formation of the West Qinling Orogen is attributed to the prolonged subduction of the Proto-Tethys Ocean and the subsequent collision between the North China Craton and the Qinling microplate along the Shangdan suture in the middle Paleozoic. The early Mesozoic subduction of the Paleo-Tethys Ocean and the subsequent collision between the Qinling terrane and the Yangtze Craton along the Mianlue suture also significantly contributed to its development (Meng QR and Zhang GW, 1999; Dong YP et al., 2011a, 2011b; Wang Y et al., 2019).

The West Qinling Orogen is subdivided into northern and southern segments by the Hezuo-Lintan-Liangdang fault (Fig.1; Zhang ZP et al., 2018; Wu YF et al., 2019a). The northern segment is dominated by abundant Devonian low- to intermediate-grade greenschist-facies metamorphic flysch sequences (Mattauer M et al., 1985; Mao JW et al., 2002). In contrast, the southern segment comprises Triassic turbidite and a minor proportion of Cambrian-Devonian strata, with no or low-grade metamorphism. During the Triassic orogeny, these strata were subjected to intense deformation, resulting in southward-dipping nappe-style thrusts (Zhang GW et al., 2001; Chen YJ and Santosh M, 2014). Precambrian basements are rarely exposed in the West Qinling Orogen, primarily south of the Mianlue suture zone. These strata are represented by the Neoproterozoic Bikou Group, which consists of a greenschist-facies sedimentary-volcanic sequence comprising basalts, basaltic tuffs, rhyolites, and rhyolitic tuffaceous sandstones (He CG et al., 2022). Zircon U-Pb dating of the meta-volcanic rocks yields ages of 840 Ma to 776 Ma, although their tectonic setting remains debated, with interpretations suggesting either an island arc environment or continental rift setting (Xia LQ et al., 2007; Zhang HF et al., 2007a, b).

Igneous intrusions are widespread in the northern portion of the West Qinling Orogen (Fig. 1). They are related to the northward subduction of the Paleo-Tethys Ocean plate (250–235 Ma), subsequent syn-collisional events (228–215 Ma), and a postcollisional phase (215–185 Ma) following the convergence of the North China Craton and the Yangtze Craton (Zeng QT et al., 2014; Dong YP and Santosh M, 2016; Qiu KF et al., 2018). Intrusions from the Late Jurassic to Early Cretaceous are scarce in the West Qinling Orogen (Fig. 1). Numerous metal deposits, including Au, Sb, Pb-Zn, and Cu-Co deposits, are distributed throughout the West Qinling Orogen in Cambrian to Triassic metamorphic strata (Mao JW et al., 2002; Chen YJ et al., 2004).

3. Deposit geology

The Xiji Cu-Co deposit is located in the northern segment of the West Qinling Orogen (Fig. 1), geographically located in the Longnan of Gansu Province. Preliminary exploration has identified 2000 t of Cu with grades of 1.59×10^{-2} and an estimated 120 t of Co with grades of 0.1×10^{-2}. The ore district is situated in the southern limb of the Xiangshan-Luoyu syncline, covered by the medium Devonian Xihanshui Formation, which consists of slate, crystalline limestone, and carbonaceous phyllitic slate (Fig. 2). Although magmatic rocks are exposed in the area, they are not directly related to the mineralization of the cobalt deposit. Drill core evidence indicates the presence of two mafic dikes at subsurface depths of approximately 20 m (M1) and 50 m (M2), respectively, with widths ranging from 2 m to 3 m.

The structure at Xiji is dominated by nearly EW-trending brittle-ductile shear zones and NW-trending faults. The EW-trending brittle-ductile shear zones are the major ore-controlling structures, extending approximately 1000 m long. They are characterized by a prevalence of altered rock, ductile shear slate, and calcite veins along the contact zone between carbonaceous phyllitic slate and crystalline limestones (Fig. 3a). The footwall of the brittle-ductile shear zone is a left-lateral strike-slip fault, which generally strikes 120°–175° with dip angles of 65°–85° and locally cuts the ductile shear slates (Figs. 3c, d). The NW-trending faults formed later and typically cut through strata and orebodies (Fig. 2). The minor strike change of the fault causes the bending of the fault plane and local stress in the bends, which has affected the location of orebodies (Figs. 2b, 3g).

The orebody is stratified, lens-shaped, and veined. The ores are predominantly composed of ductile shear slates and altered rocks, with a few ore-bearing veins in the left-lateral strike-slip fault (Figs. 3b, e). The strike and dip of the ore-bearing veins are consistent with those of the brittle-ductile shear zone. Ductile shear slates exhibit the highest Co enrichment, with peak grades of 0.29×10^{-2}. Abundant erythrite is visible in the fissures of the altered rocks and slate (Figs. 3b, d–f). Common metal minerals consist of cobaltite, chalcopyrite, and pyrite, followed by erythrite, galena, bornite, chalcocite, covellite, hematite, and malachite. Quartz, calcite, and sericite are the main gangue minerals, with minor chlorite, ankerite, and trace amounts of monazite, barite, and apatite. Co mineralization occurs primarily as disseminated

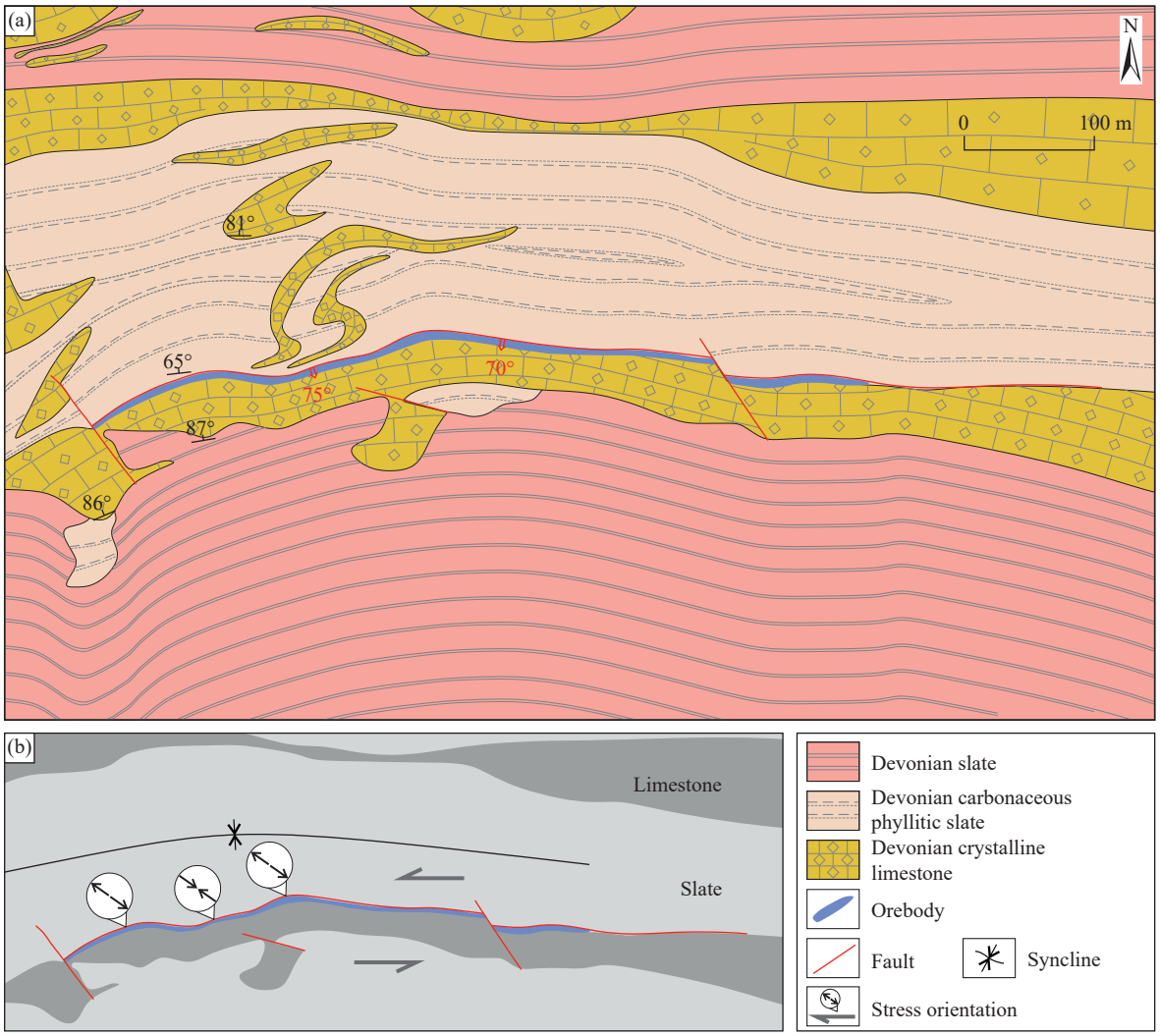


Fig. 2. a–Geological map of the Xiji Cu-Co deposit (modified from DRCCGS, 2023); b–Schematic maps showing stress condition change and a spatial relationship between structure and mineralization.

cobaltite, associated with pyrite, sericite, and calcite (Figs. 4b–d). The calcite veins exhibit significant deformation, with S-C fabric being evident (Figs. 4a, b). The alteration involved silicification, carbonation, sericitization, and sulfidation (Fig. 4). Cu mineralization is associated with silicification and pyritization (Fig. 4e), and Co mineralization is associated with sericitization, carbonation, silicification, and pyritization (Figs. 4d, g).

Four mineralization stages are distinguished based on the cutting relationship of ore veins, ore textures, and structures, as well as mineral paragenetic assemblages: Pre-mineralization, Cu mineralization, Co mineralization, and post-mineralization stages (Fig. 5). The pre-mineralization stage is characterized by the extensive development of sedimentary-type pyrite, predominantly occurring as framboidal textures and partly encased in the later pyrite, chalcopyrite, and cobaltite (Fig. 4d). The Cu mineralization stage is characterized by a quartz-chalcopyrite-pyrite assemblage, with minor bornite, chalcocite, and covellite and trace amounts of barite and monazite (Figs. 4e, f). Chalcopyrite was cut by calcite veins in the Co mineralization stage (Fig. 4f). The Co mineralization stage is characterized by a calcite-cobaltite-pyrite-sericite assemblage, with minor quartz and ankerite (Figs. 4c, d, g). Cobaltite occurs as the marginal overgrowth around early-stage pyrite. It partially filled the microfractures of the early-stage pyrite. The post-mineralization stage comprises calcite, hematite, and altered products of early cobaltite and chalcopyrite (e.g., erythrite, malachite), representing an oxidative hydrothermal event (Figs. 4h, i).

4. Sampling and analytical methods

4.1. Sample description and preparation

Representative ore and drill core samples were collected from the Xiji Cu-Co deposit, and drill core samples were obtained from the adjacent Dengjiagou Cu-Co deposit for comparison. The Dengjiagou Cu-Co deposit is situated approximately 2 km south of Xiji, with its orebody controlled by a nearly EW-trending fault. Pyrite and chalcopyrite from the pre-, Cu, and Co mineralization stages were obtained from three ore samples from Xiji, from four drill core samples from Dengjiagou, and from two mafic dikes for *in situ* sulfur

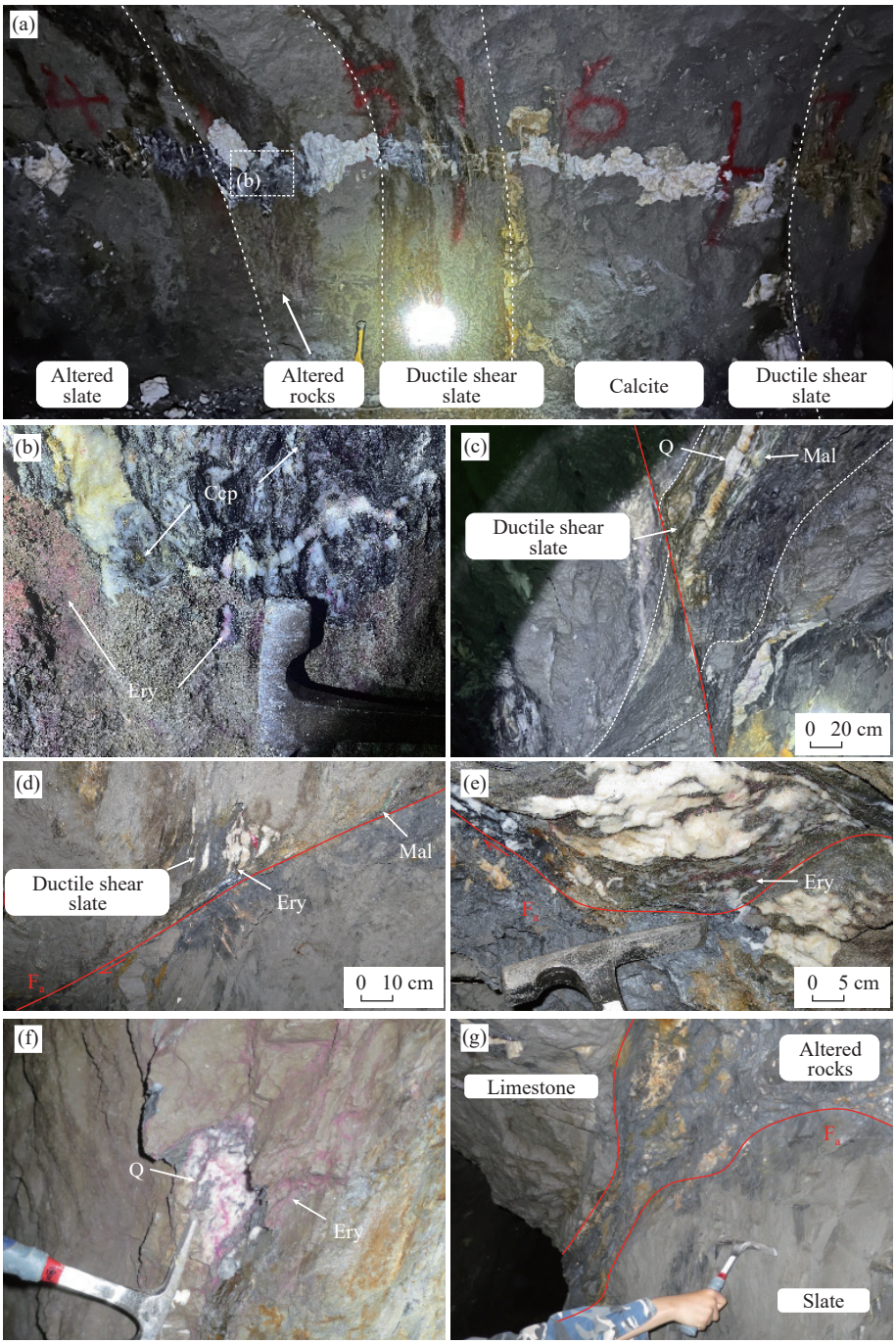


Fig. 3. Field photographs of the Xiji Cu-Co deposit. a–Section of EW-trending ore-controlling structures, containing alterated rocks, ductile shear slate, and calcite vein; b–chalcopyrite and erythrite occur within alterated rocks; c–malachite and quartz veins occur within ductile shear slate; d–ductile shear slate containing erythrite and malachite is cut by ore-controlling fault; e–erythrite, calcite veins, and quartz veins occur within ductile shear slate; f–ore-controlling fault interface is rich in erythrite; g–ore-controlling fault exhibit local dilation zones that structurally constrain the ore bodies. Ccp–chalcopyrite; Ery–erythrite; Mal–malachite; Q–quartz.

isotope analysis. Calcite veins from the pre-, Cu, and Co mineralization stages were obtained from one ore sample in Xiji for *in situ* strontium isotope analysis (Fig. 6). Pyrite from the pre-, Cu, and Co mineralization stages was obtained from three ore samples from Xiji, from one drill core sample from Dengjiagou, and from two mafic dikes for electron probe microanalysis. Doubly polished thin sections were prepared for petrographic analysis and examined under a standard optical microscope to investigate the texture, chemistry, and mineral composition of the minerals. Backscattered electron (BSE) imaging was performed using a scanning electron microscope (SEM) to characterize the microscale textures of cobaltite, pyrite, chalcopyrite, and associated minerals.

4.2. Electron probe microanalysis of pyrite

The geochemical compositions of pyrite grains in the doubly polished thin sections were determined using a JEOL JXA-8100 electron probe microanalyzer (EMPA) at the Beijing Research Institute of Uranium Geology. The

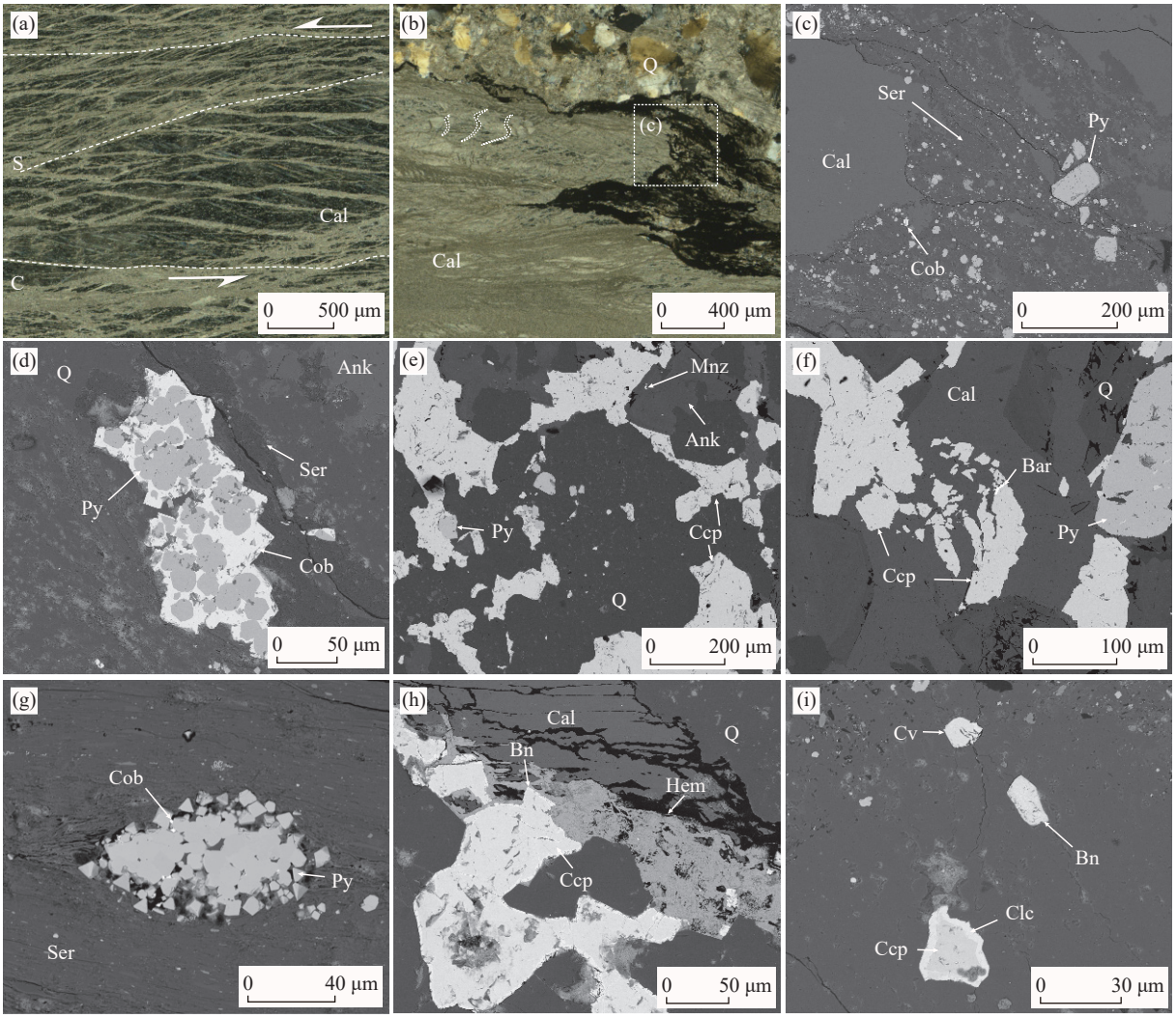


Fig. 4. Representative photomicrographs under double-polarized transmitted light (a, b) and BSE images (c–i), showing morphology parameters and mineral assemblages of four mineralization stages in the Xiji Cu-Co deposit. a–calcite are characterized by an S-C structural fabric; b–ductile shearing deformation occurs within calcite during the Co mineralization stage; c–cobaltite intergrown with sericite and pyrite in the Co mineralization stage; d–pyrite in the pre-mineralization stage enclosed by cobaltite and coexists with sericite; e–mineral assemblage comprises quartz, chalcopyrite, and pyrite in the Cu mineralization stage; f–chalcopyrite in the Cu mineralization stage was cut by calcite veins; g–pyrite in the pre-mineralization stage with microfractures filled by cobaltite and pyrite in the Co mineralization stage; h–chalcopyrite intergrown with bornite and hematite in the post-mineralization stage; i–mineral assemblage comprises chalcocite, bornite, and covellite in the post-mineralization stage. Ank–ankerite; Bar–barite; Bn–bornite; Cal–calcite; Ccp–chalcopyrite; Clc–chalcocite; Cob–cobaltite; Cv–covellite; Hem–hematite; Mnz–monazite; Py–pyrite; Q–quartz; Ser–sericite.

equipment was operated at an acceleration voltage of 20 kV, a probe current of ca. 10 nA, an electron beam of 1 μm diameter, and 20 s counting time. The following standards were used: Synthetic bismuth selenide (Se-Lα), natural skutterudite (As-Kα, Co-Kα, Ni-Kα), natural marcasite (Fe-Kα, S-Kα), natural chalcopyrite (Cu-Kα), synthetic pure germanium (Ge-Lα), synthetic zirconium anhydride (Zr-Lα), natural galena (Pb-Mα), synthetic antimony telluride (Te-Lα, Sb-Lα), natural crocoite (Cr-Kα), natural rutile (Ti-Kα), and natural buchstamite (Mn-Kα). The embedded system in the EMPA was used for ZAF correction of the EPMA data.

4.3. Electron probe and electron backscatter mapping of pyrite

LA-ICP-MS analysis was not possible due to the small size of pyrite grains, typically less than 100 μm. Consequently, electron probe and BSE imaging were utilized. Electron probe mapping was performed using a JEOL JXA-8100 EMPA at the Beijing Research Institute of Uranium Geology. Element maps were created by analyzing sets of parallel line rasters in a grid across the sample. An electron beam of 1 μm and a counting time of 10 ms, and an electron beam of 1 μm and a counting time of 12 ms were chosen for the pyrite from two ore samples (HHQ-5 and HHQ), respectively.

Electron backscatter mapping was conducted using a FEI-FEG 650 SEM equipped with an Oxford X-MAX energy dispersive spectrometer (EDS) at the School of Earth and Space Sciences, Peking University. An accelerating voltage of 15 keV, a spot size of 1 μm, and a counting time of 50 μs were chosen for the pyrite. Images were acquired and

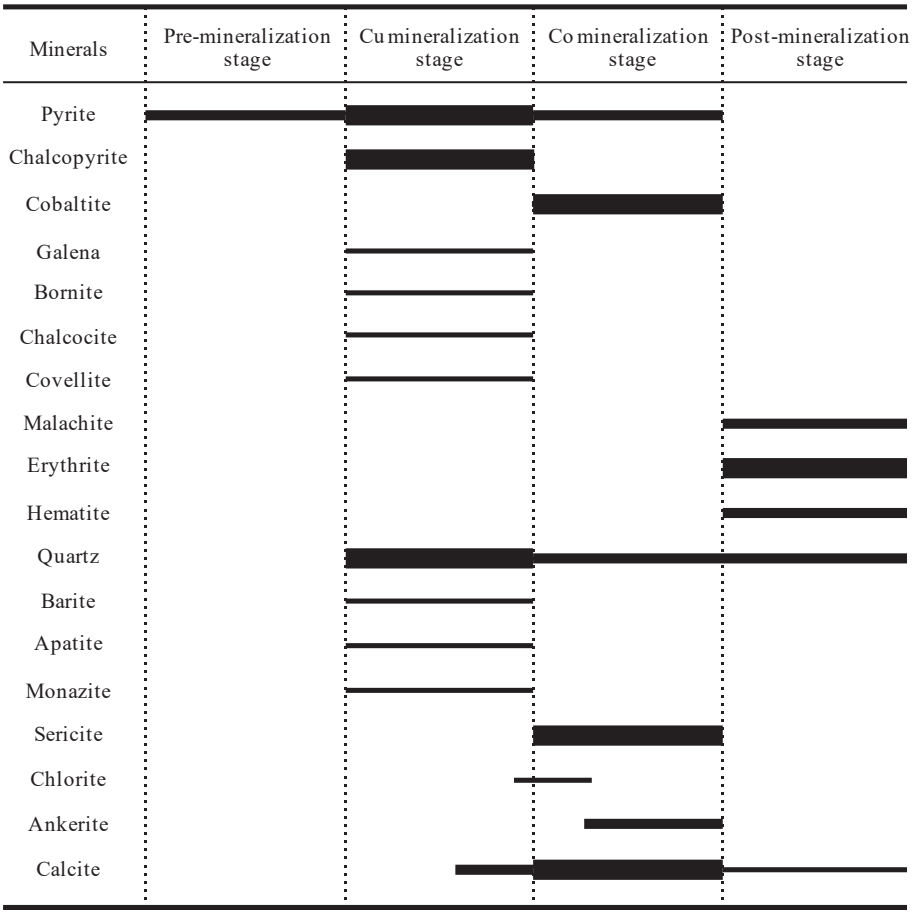


Fig. 5. Paragenetic sequence of ore-related minerals in the Xiji Cu-Co deposit. The widths of the solid lines denote relative abundance of minerals.

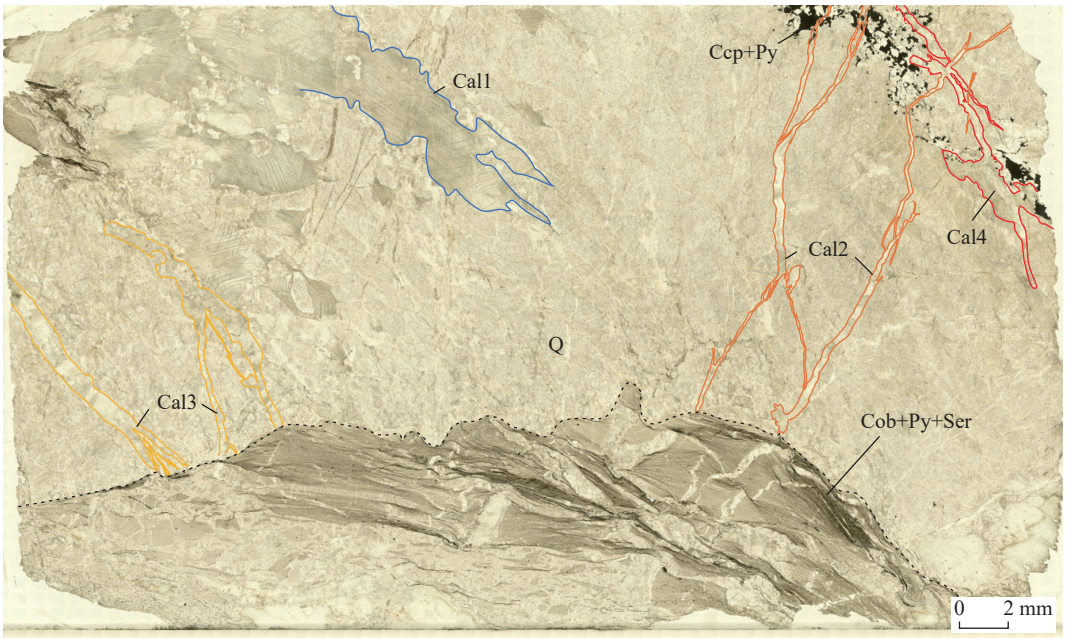


Fig. 6. Representative photomicrographs showing calcite veins and mineral assemblages of Cu and Co mineralization stages in the Xiji Cu-Co deposit. Cal1 formed concurrently with the quartz vein during the Cu mineralization stage. Cal2 and Cal3 were formed interstitially between the Cu and Co mineralization stages, which cut through chalcopyrite and subsequently cut by the alteration mineral assemblage of the cobalt mineralization stage. Cal4 was formed in Co mineralization stage, cutting through Cal2. Cal–calcite; Ccp–chalcopyrite; Cob–cobaltite; Py–pyrite; Q–quartz; Ser–sericite.

processed using the program Aztec.

4.4. In situ LA-MC-ICP-MS S isotope analysis of sulfides

The *in situ* sulfur isotope analysis of pyrite was carried out using LA-MC-ICP-MS at the Kehui Test Technology Co., Ltd., Tianjin. The system comprised a Resolution SE 193 nm solid-state laser ablation system coupled with a Neptune Plus MC-ICP-MS. The laser fluence was 3 J/cm^2, the frequency was 5 Hz, the spot size was 24 μm, the denudation model was single-point denudation, the carrier gas was high-purity He (420 mL/min), and the supplementary gas was Ar (0.85 L/min). The ^{32}S and ^{34}S isotopes were obtained using a Faraday cup measurement system with an integral time of 0.131 s and a background collection time of 27 a; 200 datapoints were obtained. Before the test, the instrument parameters were adjusted with the sulfide standard sample. Sulfides similar to the sample matrix were used as standard samples to reduce the matrix effect on the test results. The standard sample, standard cross method was used to correct the results. The standard samples were JX and ZX. All laboratory standards for analyzing the sulfur isotopes were obtained using stable gas isotope mass spectrometry or MC-ICP-MS via solution injection. The δ^{34}S values were calculated using the standard-sample bracketing (SSB) calibration method: $\delta^{x}S = [(^{x}S/^{32}S_{sample})/(^{x}S/^{32}S_{standard}) - 1] * 1000$; X is 34 or 33. The $^{34}S/^{32}S_{standard}$ is the mean isotope ratio of the two standard samples, which is measured once before and after sample analysis.

4.5. In situ LA-MC-ICP-MS Sr isotope analysis of calcite

The Sr isotope ratio of calcite was measured using a Neptune Plus MC-ICP-MS (Thermo Fisher Scientific, Bremen, Germany) equipped with a Geolas HD excimer ArF laser ablation system (Coherent, Göttingen, Germany) at the Wuhan Sample Solution Analytical Technology Co., Ltd., Hubei, China. The Neptune Plus was equipped with nine Faraday cups fitted with 10^{11} Ω resistors. The Faraday collector configuration of the mass system consisted of an L4 to H3 array to monitor Kr, Rb, Er, Yb, and Sr. The combination of the high-sensitivity X-skimmer cone and the Jet-sample cone was employed. In the laser ablation system, helium was used as the carrier gas for the ablation cell. The spot diameter for a single laser spot ablation ranged from 60 μm to 160 μm and depended on the Sr signal intensity. The pulse frequency was 8 Hz to 15 Hz, but the laser fluence was kept constant at 10 J/cm^2. A new signal smoothing device (Hu ZC et al., 2015) was used downstream from the sample cell to eliminate the short-term variation of the signal. All data reduction in the MC-ICP-MS analysis of Sr isotope ratios was conducted using Iso-Compass software (Zhang L et al., 2020). The interference correction strategy used by Tong XR et al. (2016) and Zhang W et al. (2018) was employed. The regions of integration for the gas background and the sample were selected. No Kr peak stripping was applied after the background correction, which removes the background Kr^+ signals. Interferences were corrected as follows: (1) The interferences of $^{168}Er^{++}$ on ^{84}Sr, $^{170}Er^{++}$ and $^{170}Yb^{++}$ on ^{85}Rb, $^{172}Yb^{++}$ on ^{86}Sr, and $^{174}Yb^{++}$ on ^{87}Sr were corrected based on the measured signal intensities of $^{167}Er^{++}$ and $^{173}Yb^{++}$ and the natural isotope ratios of Er and Yb (Berglund M and Wieser ME, 2011); (2) the isobaric interference of ^{87}Rb on ^{87}Sr was corrected by monitoring the ^{85}Rb signal intensity and a user-specified $^{87}Rb/^{85}Rb$ ratio using an exponential law for mass bias. The user-specified $^{87}Rb/^{85}Rb$ ratio was calculated by measuring reference materials, BCR-2G (USGS glasses), with a known $^{87}Sr/^{86}Sr$ ratio. Following the interference corrections, the mass fractionation of Sr isotopes was corrected by assuming $^{88}Sr/^{86}Sr = 8.375209$ (Tong XR et al., 2016; Zhang W et al., 2018) and applying the exponential law.

5. Results

5.1. Geochemical composition of pyrite

A total of 47 EPMA spot analyses were performed on pyrite grains representing mafic dikes and the pre-, Cu, and Co mineralization stages. The chemical compositions of the selected pyrite grains from Xiji are shown in Table 1 and Fig. 7.

The EPMA analysis indicates a narrow range of the S content across different generations of pyrite (52.65% to 54.07%). Each pyrite generation has a different Fe content range, with a narrower range in the pre-mineralization stage (45.61% to 46.27% in slate, 45.86% to 46.67% in limestone) than in the mineralization stage (44.38% to 46.46% in the Cu mineralization stage and 44.43% to 46.89% in the Co mineralization stage). The Co content range differs for different pyrite generations. The pyrite in the pre-mineralization stage has a slightly lower Co content, ranging from 0.07% to 0.13% in slate and from 0.07% to 0.1% in limestone. The pyrite in the Cu and Co mineralization stages exhibits a slightly higher Co content, ranging from 0.1% to 0.41% and 0.02% to 0.37%, respectively. The As content in pyrite differs across the stages, with pyrite in slate having a narrower range (0.03% to 0.26%). Conversely, the pyrite from limestone, as well as that in the Cu and Co mineralization stages, has a wide range, and the content is sometimes below the detection limit. The As content of pyrite in limestone and that in the Cu mineralization stage range from 0.03% to 0.38% and 0.05% to 0.53%, respectively. Notably, the pyrite in the Co mineralization stage has a relatively high As content (0.08% to 0.96%).

The S content of pyrite in the two mafic dikes has a narrow range (52.93% to 53.47% and 53.25% to 53.77%, respectively). However, the Fe content of pyrite differed between the two mafic dikes (43.98% to 46.15% and 45.89% to 46.61%, respectively). The pyrite in the two mafic dikes exhibits a relatively high Co content (0.05% to 2.27% and 0.03% to 0.15%, respectively). It has a relatively low As content, often below the detection limit, ranging from 0.01% to 0.02% and 0.01% to 0.07%, respectively.

Table 1. Geochemical Compositions of Pyrite in the Xiji Cu-Co Deposit (wt%).

Sample		Sample description	Se	As	Fe	S	Ge	Co	Zr	Ni	Te	Cr	Pb	Cu	Sb	Ti	Mn	Total
HHQ	1	Slate	0.03	0.26	45.61	52.91	0.04	0.09	0.11	/	0.04	0.04	0.19	/	/	0.05	/	99.37
	2	Co mineralization stage	/	0.11	46.08	53.2	0.04	0.12	/	0.02	/	/	0.1	/	/	/	/	99.67
	3	Slate	/	0.11	46.14	52.81	/	0.1	/	/	/	/	0.23	/	/	/	0.02	99.41
	4	Slate	/	0.19	45.64	53.3	/	0.13	/	0.02	0.03	/	0.21	0.05	/	0.03	/	99.6
	5	Cu mineralization stage	/	0.49	44.63	53.98	0.02	0.39	/	/	/	/	0.1	/	0.06	/	/	99.67
	6	Cu mineralization stage	/	0.53	44.38	53.79	0.05	0.41	/	0.04	/	/	0.15	0.09	0.04	/	0.05	99.53
	7	Cu mineralization stage	/	/	46.46	53.35	0.03	0.1	0.06	/	/	/	/	/	/	/	/	100
	8	Cu mineralization stage	/	0.08	44.43	54.07	/	0.37	/	/	/	/	0.33	/	/	0.02	/	99.3
HHQ-5	1	Slate	/	0.21	46.08	53.4	/	0.11	/	/	0.03	/	0.12	/	/	/	/	99.95
	2	Slate	/	0.12	45.99	53.11	/	0.08	/	/	/	0.03	0.22	0.04	0.03	0.05	/	99.67
	3	Slate	/	0.04	46.18	52.93	/	0.09	/	0.02	/	/	0.09	/	/	/	/	99.35
HHQ-6	1	Cu mineralization stage	/	0.1	45.92	52.97	/	0.14	/	/	/	/	0.1	/	/	/	/	99.23
	2	Cu mineralization stage	0.05	/	45.87	52.99	/	0.1	/	/	/	/	0.32	0.03	/	0.07	/	99.43
	3	Slate	/	0.03	46.2	52.81	/	0.1	/	/	0.09	0.02	/	/	/	/	/	99.25
	4	Co mineralization stage	/	0.05	45.72	52.75	0.05	0.1	/	/	/	/	0.18	/	/	/	/	98.85
	5	Co mineralization stage	/	/	46.04	53.27	/	0.06	/	0.02	/	0.02	0.15	/	/	/	0.04	99.6
	6	Co mineralization stage	/	/	45.88	52.93	/	0.09	/	/	/	0.02	0.1	/	0.04	/	/	99.06
	7	Limestone	/	0.03	46.16	53.28	0.03	0.09	0.04	/	/	/	/	/	/	/	0.03	99.66
	8	Limestone	/	/	46.59	53.36	/	0.07	/	/	/	/	0.09	/	/	/	/	100.11
	9	Limestone	/	/	46.3	53.32	/	0.08	/	/	/	/	0.16	/	0.03	/	/	99.89
	10	Slate	/	0.09	46.27	52.77	/	0.07	/	/	0.03	/	0.17	/	/	/	/	99.4
DJG-02	1	Mafic rocks-M1	/	/	46.15	52.93	/	0.06	0.02	/	/	/	/	/	/	/	/	99.16
	2	Mafic rocks-M1	/	/	45.71	52.96	/	0.09	0.01	/	/	/	/	/	/	/	0.01	98.78
	3	Mafic rocks-M1	/	0.01	45.71	53.3	/	0.06	/	/	/	0.01	/	0.01	/	/	/	99.1
	4	Mafic rocks-M1	/	/	44.87	53.28	/	0.22	/	1.07	0.01	0.02	/	/	/	/	/	99.47
	5	Mafic rocks-M1	/	/	45.79	53.32	/	0.07	/	/	/	/	/	0.02	/	0.01	0.02	99.23
	6	Mafic rocks-M1	/	0.02	43.98	53.33	/	2.27	/	/	0.01	/	/	/	/	/	/	99.61
	7	Mafic rocks-M1	0.01	/	45.24	53	/	0.15	/	0.86	/	/	/	0.04	/	0.06	/	99.36
	8	Mafic rocks-M1	/	0.01	45.47	53.41	/	0.15	/	0.04	0.03	/	/	0.01	0.01	/	/	99.13
	9	Mafic rocks-M1	/	/	46.08	53.47	/	0.05	/	0.02	0.01	0.01	/	0.01	/	/	/	99.65
DJG-03	1	Limestone	/	0.38	46.12	53.31	/	0.1	0.01	/	/	0.02	/	/	/	/	/	99.94
	2	Limestone	/	/	45.86	52.87	/	0.05	/	0.03	/	/	/	/	/	0.02	/	98.83
	3	Limestone	0.01	0.03	46.67	53.54	/	0.06	/	/	0.01	0.04	/	0.02	/	0.01	0.01	100.4
	4	Co mineralization stage	/	0.96	45.95	52.71	/	0.04	/	/	/	0.03	/	0.03	/	0.04	/	99.76
	5	Co mineralization stage	/	0.08	46.12	53.51	0.01	0.07	0.01	/	/	0.02	/	/	/	/	/	99.82
	6	Co mineralization stage	/	0.79	46.03	52.84	0.01	0.02	/	/	/	/	/	0.02	0.02	0.01	0.01	99.75
	7	Co mineralization stage	/	0.2	46.17	52.65	/	0.07	0.01	/	/	/	/	/	/	0.05	/	99.15
	8	Co mineralization stage	/	0.11	46.89	53.2	/	0.07	0.02	/	/	0.01	/	0.01	/	/	0.03	100.34
	9	Co mineralization stage	/	0.26	46.11	53.01	/	0.04	/	/	/	/	/	/	/	/	/	99.42
DJG-05	1	Mafic rocks-M2	/	0.03	45.94	53.55	/	0.12	/	/	/	/	/	/	/	0.04	/	99.68
	2	Mafic rocks-M2	/	0.07	46.03	53.55	/	0.09	/	0.08	/	0.01	/	/	/	/	/	99.83
	3	Mafic rocks-M2	0.01	/	46.24	53.77	/	0.14	/	/	/	0.02	/	0.01	/	/	0.01	100.2
	4	Mafic rocks-M2	/	0.01	46.46	53.44	/	0.15	0.03	0.03	/	0.01	/	/	0.02	/	0.01	100.16
	5	Mafic rocks-M2	/	0.02	45.94	53.26	/	0.07	/	0.02	0.02	/	/	/	0.01	/	/	99.34
	6	Mafic rocks-M2	/	/	46.61	53.43	/	0.03	/	/	/	0.01	/	/	0.02	/	/	100.1
	7	Mafic rocks-M2	0.01	/	45.89	53.38	/	0.07	0.03	/	/	0.03	/	/	/	0.04	/	99.45
	8	Mafic rocks-M2	/	/	46.45	53.25	/	0.09	/	/	/	0.02	/	/	0.01	/	/	99.82

5.2. Electron probe and electron backscatter maps of pyrite

The evolution of pyrite-forming fluids was recorded by successive pyrite formations. The spatial variations of the S isotopes and the relative abundances of trace elements in the pyrite grains derived from electron probe and electron backscatter analysis are shown in Figs. 8, 9. The electron probe maps demonstrate low Co and As concentrations in the pyrite in the pre-mineralization stage. A negative correlation exists between the Co and Ni concentrations in cobaltite (Fig. 8). The electron backscatter map shows that the trace elements in the different growth zones in the pre-mineralization stage pyrite remain unchanged. Conversely, the outer rim of the pyrite exhibits signs of alteration by ore-forming fluids in the mineralization stage. This area is enriched in As, Mg, and Se (Fig. 9).

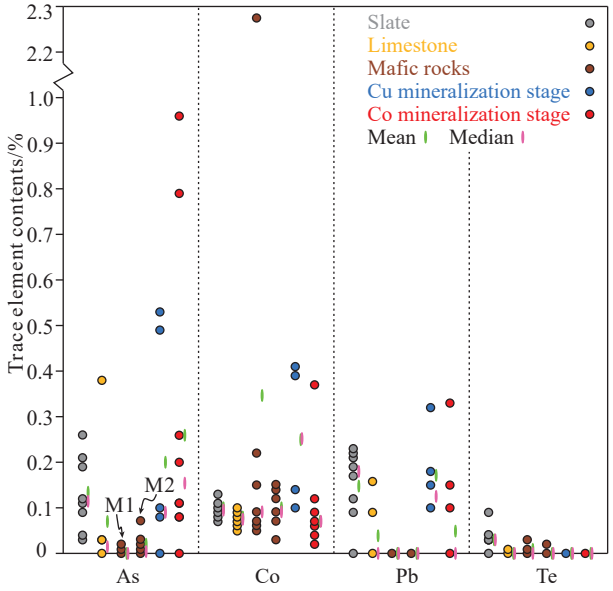


Fig. 7. Plots of trace element contents for the pyrite acquired by EMPA analysis from the Xiji Cu-Co deposit. The spot at 0 indicates the value below the detection limit.

5.3. Result of in situ S isotope analysis

The LA-ICP-MS *in situ* sulfur isotope data of pyrite and chalcopyrite from the Xiji and the Dengjiagou and the pyrite from two mafic dikes are summarized in Table 2 and Figs. 10, 11. The $\delta^{34}S$ values of pyrite in the Cu and Co mineralization stages have narrow ranges and exhibit notable disparities. The Cu mineralization-stage pyrite and chalcopyrite from Xiji have $\delta^{34}S$ values ranging from +6.19‰ to +10.16‰ (n=8, average +8.14‰; Figs. 10b, g) and +5.92‰ to +7.02‰ (n=6, average +6.42 ‰), respectively. The Cu mineralization-stage pyrite from Dengjiagou has $\delta^{34}S$ values ranging from +5.41‰ to +7.29‰ (n=3, average +6.79‰). Notably, the Co mineralization stage pyrite from Xiji and Dengjiagou has $\delta^{34}S$ values ranging from +5.69‰ to +27.44‰ (n=10, average +11.39‰; Fig. 10c) and +10.11‰ to +12.30‰ (n=14, average +11.42‰; Fig. 10d), respectively. The pre-mineralization-stage pyrite in the slate has $\delta^{34}S$ values ranging from −31.67‰ to −1.08‰ (n=17, average −18.56‰, Fig. 10a). In contrast, that in the limestone ranges from +13.54‰ to +18.58‰ (n=5, average +15.87‰) and +14.08‰ to +17.95‰ (n=4, average +15.97‰; Fig. 10d), respectively. The pyrite from the two mafic dikes has $\delta^{34}S$ values ranging from +3.90‰ to +7.30‰ (M1, n=11, average +5.99‰; Fig. 10f) with an anomalous value of −12.45‰ and +2.61‰ to +3.21‰ (M2, n=8, average +2.85‰; Fig. 10e), respectively.

5.4. Results of in situ Sr isotope analysis

The LA-ICP-MS *in situ* strontium isotope data of calcite from Xiji are summarized in Table 3. The $^{87}Sr/^{86}Sr$ values of the 36 spots range from 0.709347 to 0.711368, with an average of 0.709930. Cal1, Cal2, and Cal3 show minimal variation in the $^{87}Sr/^{86}Sr$, with ranges of 0.709664 to 0.710227 (n=7, average 0.709869), 0.709478 to 0.709865 (n=10, average 0.709638), and 0.709347 to 0.710291 (n=7, average 0.709756), respectively. In contrast, Cal4 has a wider range of $^{87}Sr/^{86}Sr$, showing a different isotopic composition of radioactive strontium, ranging from 0.709627 to 0.711368 (n=12, average 0.710311).

6. Discussion

6.1. Hydrothermal origin of cobaltite

The Co in the deposits exists in two forms. (1) Independent cobalt-bearing minerals, encompassing sulfides, arsenides, and oxides, e.g., linnaeite (Co_3S_4), cattierite (CoS_2), cobaltite (CoAsS), siegenite ($(Co,Ni)_3S_4$), and spherocobaltite ($CoCO_3$); (2) isomorphic substitution for Mn, Fe, Cu, and Ni in oxides and sulfides. The substitution results in common cobalt-rich minerals, such as pyrite, pyrrhotite, pentlandite, polydymite, and gersdorffite, among others (Lu YG et al., 2020, 2021). In the Cu and Co mineralization stages of the Xiji deposit, only a fraction of the pyrite displayed elevated Co contents (Fig. 7), indicating that cobaltite is the primary cobalt-bearing mineral in the deposit, and some of the pyrite is Co-rich.

The pre-mineralization-stage pyrite in the slate exhibits marked As enrichment and has significantly negative $\delta^{34}S$ values (−31.67‰ to −1.08‰; Figs. 7, 12). This observation suggests the influence of bacterial sulfate reduction (BSR) and he integration of organic matter (Ding XJ et al., 2024). The high Te content in the pyrite in slate also indicates a reducing sedimentary environment (Fig. 7; Cao GS et al., 2023). Cobaltite generally occurs as an intergrowth with framboidal pyrite in slate (Fig. 8). However, the framboidal pyrite in this study exhibits a core-rim structure, and cobaltite has formed in the fractures (Fig. 8b), suggesting that cobaltite crystallized during the hydrothermal stage, not during the sedimentary stage.

6.2. Source of ore-forming fluid

In the Cu and Co mineralization stages, sulfur primarily exists as S^{2-} in sulfides, such as chalcopyrite and pyrite, with no sulfate minerals observed, indicating reducing conditions. Therefore, the $\delta^{34}S$ value of the sulfides reflects the sulfur isotope characteristic of the ore fluid (Ohmoto H, 1972; Deng J et al., 2015; Sun PF et al., 2020; Wang XS et al., 2015).

Excluding outliers, the $\delta^{34}S$ values (+5.92‰ to +10.16‰ and +5.69‰ to +12.03‰) in the Cu and Co mineralization stages are in the range of the $\delta^{34}S$ values of the sedimentary rocks, granitic volcanic rocks, and meta-volcanic rocks of the Bikou Group (Fig. 12), differing significantly from those of the limestone (+13.54‰ to +18.58‰), slate (−31.67‰ to −1.08‰), and mafic dikes (+2.61‰ to +3.21‰ and +3.90‰ to +7.30‰; Fig. 12). This finding indicates that the sulfur of the ore-forming fluids does not resemble that of the mafic dikes and wall rock but has a closer affinity to that of the Bikou Group. The Bikou Group is representative of the Neoproterozoic metamorphic basement. It is predominantly

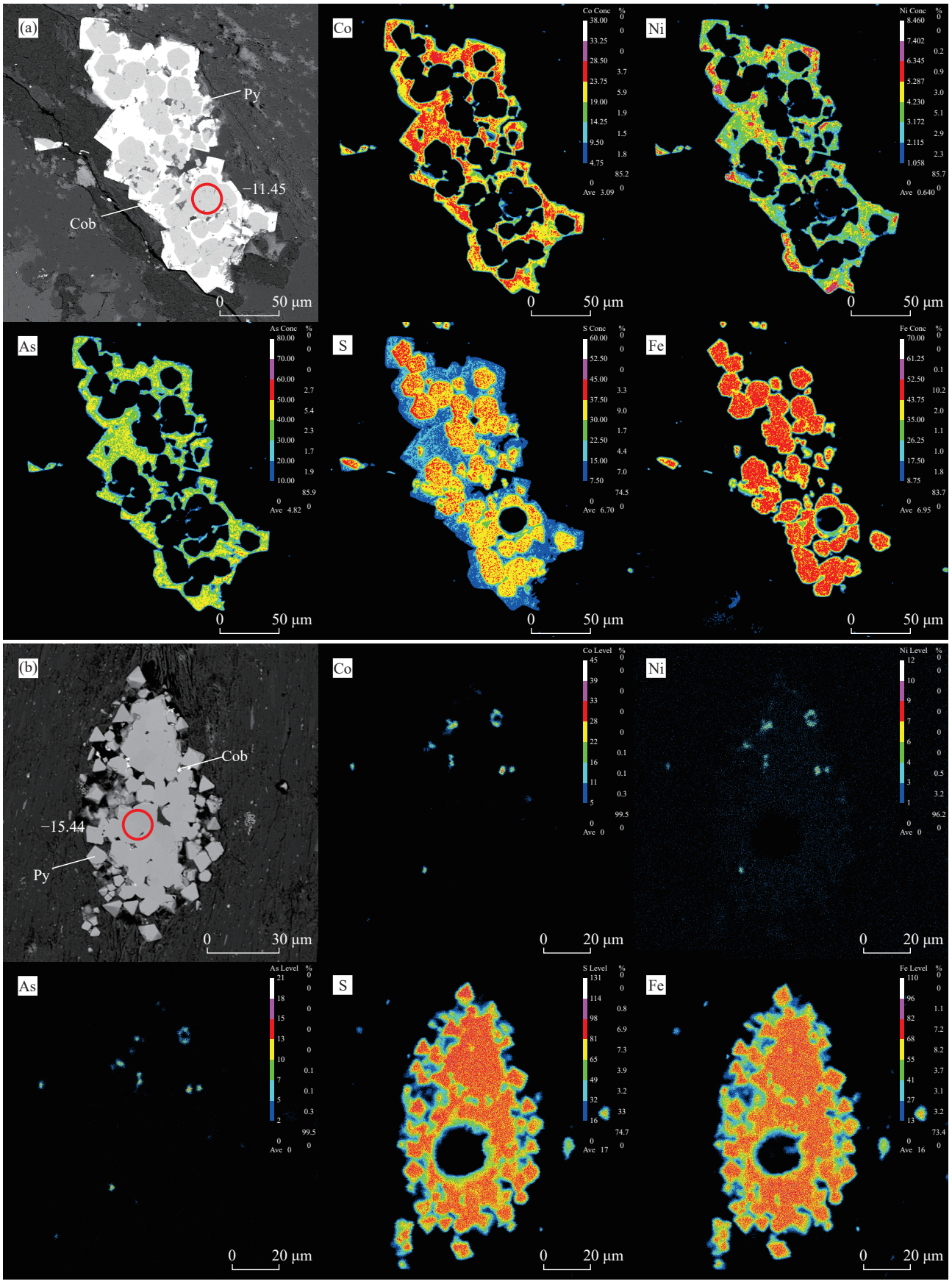


Fig. 8. Photomicrograph and electron probe maps of pyrite grains displaying intergrowth relationship between pyrite and cobaltite. a–Pyrite enclosed by cobaltite. b–pyrite with microfractures filled by cobaltite. Red circles represent the spot position for *in situ* sulfur isotope analysis and the white numbers show $\delta^{34}S$ values.

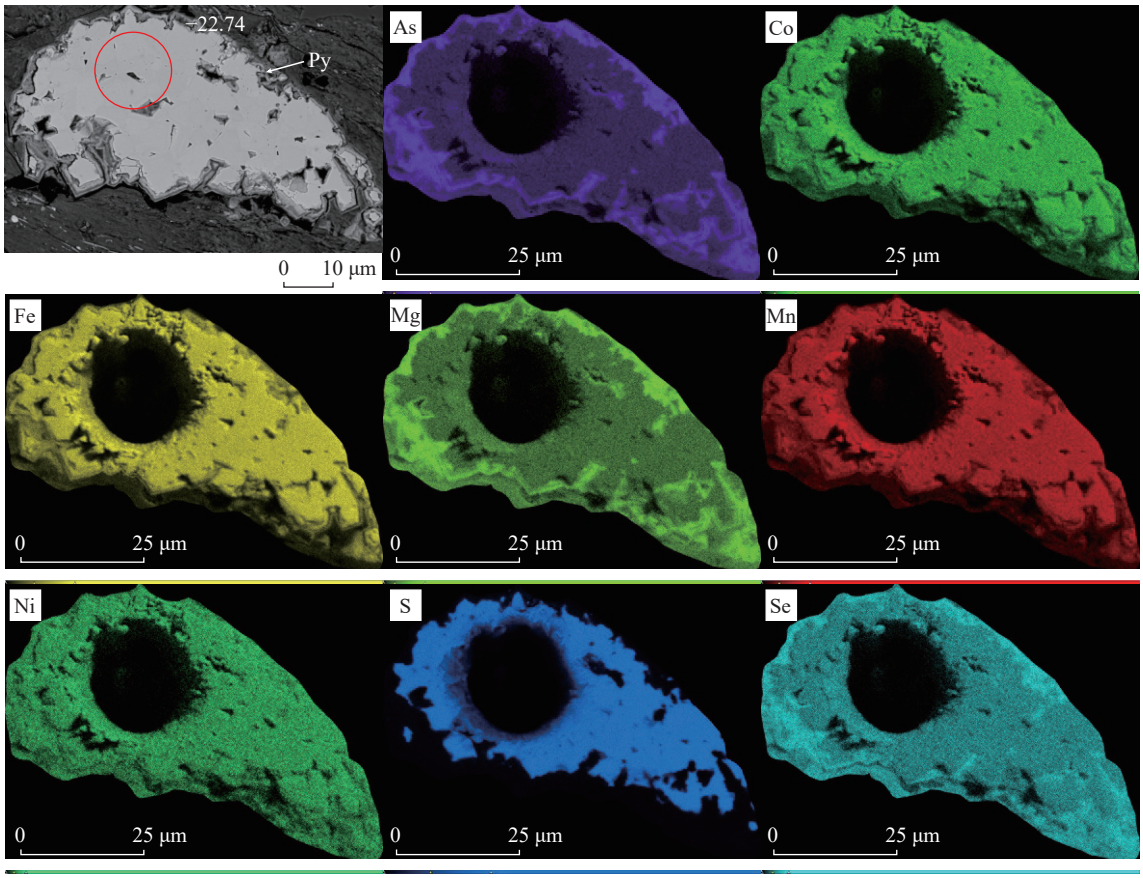


Fig. 9. Photomicrograph and electron backscatter maps of pyrite grains in the pre-mineralization stage displaying the alteration of pyrite by ore-forming fluids in the mineralization stage. Red circles represent the spot position for *in situ* sulfur isotope analysis and the white numbers show $\delta^{34}S$ values.

exposed in the southern part of the West Qinling Orogen, with few outcrops elsewhere. The widespread distribution of Triassic granites derived from the partial melting of the meta-mafic rocks in the metamorphic basement indicates a broad distribution of the metamorphic basement in the deep crust (Zhang HF et al., 2007a). The ore-forming fluids could be derived from the Neoproterozoic metamorphic basement, which has conditions similar to those of the Bikou Group beneath the Phanerozoic sedimentary cover.

Since calcite contains very low Rb concentrations, it is assumed that negligible radiogenic Sr was produced post-crystallization (Hu QQ, 2015; He CG, 2022). Furthermore, since the Sr isotopic composition of carbonate minerals is unaffected by the equilibrium temperature, the measured Sr isotopic ratios of calcite represent those of the ore-forming fluids (Kontak DJ and Kerrich R, 1995, 1997). The $^{87}Sr/^{86}Sr$ ratio of the calcite veins in the Cu and Co mineralization stages differs from that of the known strontium reservoirs in the West Qinling Orogen (Fig. 13), including Triassic granites (Zhang HF et al., 2007a; 2007b), Devonian siltstone, phyllite, limestone (Zhang L et al., 2009), Cambrian carbonaceous and siliceous sedimentary rocks (Liu JJ et al., 2014), as well as Silurian slate, dolomite, and siliceous rocks (Liu JJ et al., 2014), except for Neoproterozoic Bikou meta-volcanic rocks (Xia LQ et al., 2007; He CG, 2022), which is consistent with the S isotope results. The $\delta^{34}S$ values of pyrite and the $^{87}Sr/^{86}Sr$ ratio of calcite indicate that the metamorphic basement of the West Qinling Orogen, analogous to the Bikou Group with extensive meta-volcanic rocks dominated by meta-mafic rocks, constitutes the source for ore-forming fluids responsible for the Xiji Cu-Co deposit.

6.3. Potential sources of Co metals

Co abundance varies across the Earth's layers, with the highest concentrations in the core (approximately 2500×10^{-6}). The cobalt abundance in the primitive mantle (105×10^{-6}) is approximately 1/25 of that in the core. The abundance in the continental crust is lower, about 1/5 of that of the mantle (approximately 21×10^{-6}; Su BX et al., 2023). Experimental evidence indicates that the solubility of cobalt in mafic-ultramafic magmas is 111500×10^{-6} at 1 atm, 1400°C, and IW + 1.5 oxygen fugacity, demonstrating significant Co enrichment capacity (Holzheid A et al., 1994, 1996). The high solubility of cobalt in mafic-ultramafic magmas facilitates the migration of Co metals from the mantle to other Earth's layers, such as the metamorphic basement (Sillitoe RH et al., 2017), making these layers a potential source for Co metals. During diagenesis, the deposition of cobalt-rich materials derived from the weathering of mafic-ultramafic dikes occurs, or cobalt-rich pyrite is formed by the reaction of H_2S with dissolved Fe and Co in a semi-closed sulfide ocean basin (Qiu

Table 2. *In situ* S isotope Data of the Xiji Cu-Co deposit.

Deposit	Sample	Sample description	Analyzed material	$\delta^{34}S_{V\text{-}CDT}$ /‰
Xiji	HHQ-4-1	Limestone, Cu mineralization stage	Pyrite	6.28
	HHQ-6-4	Limestone, Cu mineralization stage	Pyrite	10.16
	HHQ-6-5	Limestone, Cu mineralization stage	Pyrite	6.19
	HHQ-6-6	Limestone, Cu mineralization stage	Pyrite	6.30
	HHQ-9	Limestone, Cu mineralization stage	Chalcopyrite	7.02
	HHQ-10	Limestone, Cu mineralization stage	Chalcopyrite	6.48
	HHQ-11	Limestone, Cu mineralization stage	Chalcopyrite	6.88
	HHQ-4-2	Limestone, Cu mineralization stage	Chalcopyrite	6.19
	HHQ-4-3	Limestone, Cu mineralization stage	Chalcopyrite	5.92
	HHQ-4-4	Limestone, Cu mineralization stage	Chalcopyrite	6.02
	HHQ-5	Slate, Cu mineralization stage	Pyrite	9.57
	HHQ-6	Slate, Cu mineralization stage	Pyrite	9.43
	HHQ-7	Slate, Cu mineralization stage	Pyrite	9.00
	HHQ-8	Slate, Cu mineralization stage	Pyrite	8.31
	HHQ-6-1	Limestone, Co mineralization stage	Pyrite	8.04
	HHQ-6-2	Limestone, Co mineralization stage	Pyrite	27.44
	HHQ-6-3	Limestone, Co mineralization stage	Pyrite	10.83
	HHQ-6-8	Limestone, Co mineralization stage	Pyrite	7.44
	HHQ-6-9	Limestone, Co mineralization stage	Pyrite	5.69
	HHQ-6-10	Limestone, Co mineralization stage	Pyrite	12.03
	HHQ-6-11	Limestone, Co mineralization stage	Pyrite	10.40
	HHQ-6-12	Limestone, Co mineralization stage	Pyrite	9.54
	HHQ-6-19	Limestone, Co mineralization stage	Pyrite	9.11
	HHQ-2	Slate, Co mineralization stage	Pyrite	10.04
	HHQ-6-13	Limestone	Pyrite	18.58
	HHQ-6-14	Limestone	Pyrite	15.34
	HHQ-6-15	Limestone	Pyrite	13.54
	HHQ-6-16	Limestone	Pyrite	16.50
	HHQ-6-17	Limestone	Pyrite	15.40
	HHQ-6-18	Slate	Pyrite	−21.46
	HHQ-6-7	Slate	Pyrite	−19.35
	HHQ-1	Slate	Pyrite	−19.96
	HHQ-3	Slate	Pyrite	−1.08
	HHQ-4	Slate	Pyrite	−11.45
	HHQ-5-1	Slate	Pyrite	−15.44
	HHQ-5-2	Slate	Pyrite	−22.74
	HHQ-5-3	Slate	Pyrite	−20.05
	HHQ-5-4	Slate	Pyrite	−15.74
	HHQ-5-5	Slate	Pyrite	−19.64
	HHQ-5-6	Slate	Pyrite	−19.51
	HHQ-5-7	Slate	Pyrite	−22.45
	HHQ-5-8	Slate	Pyrite	−21.29
	HHQ-5-9	Slate	Pyrite	−31.67
	HHQ-5-10	Slate	Pyrite	−21.89
	HHQ-5-11	Slate	Pyrite	−18.23
	HHQ-5-12	Slate	Pyrite	−13.52
Drill core	DJG-4-1	Cu mineralization stage	Pyrite	7.29
	DJG-4-2	Cu mineralization stage	Pyrite	7.66
	DJG-4-3	Cu mineralization stage	Pyrite	5.41
	DJG-3-4	Limestone, Co mineralization stage	Pyrite	11.26
	DJG-3-5	Limestone, Co mineralization stage	Pyrite	11.29
	DJG-3-6	Limestone, Co mineralization stage	Pyrite	17.00
	DJG-3-7	Limestone, Co mineralization stage	Pyrite	11.97
	DJG-3-8	Limestone, Co mineralization stage	Pyrite	10.11
	DJG-3-9	Limestone, Co mineralization stage	Pyrite	12.14
	DJG-6-1	Co mineralization stage	Pyrite	12.30
	DJG-6-2	Co mineralization stage	Pyrite	11.70
	DJG-6-3	Co mineralization stage	Pyrite	11.55

Table 2. (*Continued*)

Deposit	Sample	Sample description	Analyzed material	$\delta^{34}S_{V\text{-}CDT}$ /‰
	DJG-6-4	Co mineralization stage	Pyrite	10.87
	DJG-6-5	Co mineralization stage	Pyrite	11.79
	DJG-6-6	Co mineralization stage	Pyrite	11.70
	DJG-6-7	Co mineralization stage	Pyrite	11.10
	DJG-6-8	Co mineralization stage	Pyrite	11.04
	DJG-6-9	Co mineralization stage	Pyrite	11.05
	DJG-3-1	Limestone	Pyrite	14.08
	DJG-3-2	Limestone	Pyrite	14.86
	DJG-3-3	Limestone	Pyrite	17.95
Mafic	DJG-2-1	Mafic dikes-M1	Pyrite	6.63
	DJG-2-2	Mafic dikes-M1	Pyrite	7.30
	DJG-2-3	Mafic dikes-M1	Pyrite	6.08
	DJG-2-4	Mafic dikes-M1	Pyrite	6.40
	DJG-2-5	Mafic dikes-M1	Pyrite	6.17
	DJG-2-6	Mafic dikes-M1	Pyrite	3.90
	DJG-2-7	Mafic dikes-M1	Pyrite	6.95
	DJG-2-8	Mafic dikes-M1	Pyrite	5.45
	DJG-2-9	Mafic dikes-M1	Pyrite	6.23
	DJG-2-10	Mafic dikes-M1	Pyrite	6.77
	DJG-2-11	Mafic dikes-M1	Pyrite	4.05
	DJG-2-12	Mafic dikes-M1	Pyrite	−12.45
	DJG-5-1	Mafic dikes-M2	Pyrite	3.21
	DJG-5-2	Mafic dikes-M2	Pyrite	2.73
	DJG-5-3	Mafic dikes-M2	Pyrite	2.84
	DJG-5-4	Mafic dikes-M2	Pyrite	2.91
	DJG-5-5	Mafic dikes-M2	Pyrite	3.04
	DJG-5-6	Mafic dikes-M2	Pyrite	2.74
	DJG-5-7	Mafic dikes-M2	Pyrite	2.61
	DJG-5-8	Mafic dikes-M2	Pyrite	2.75

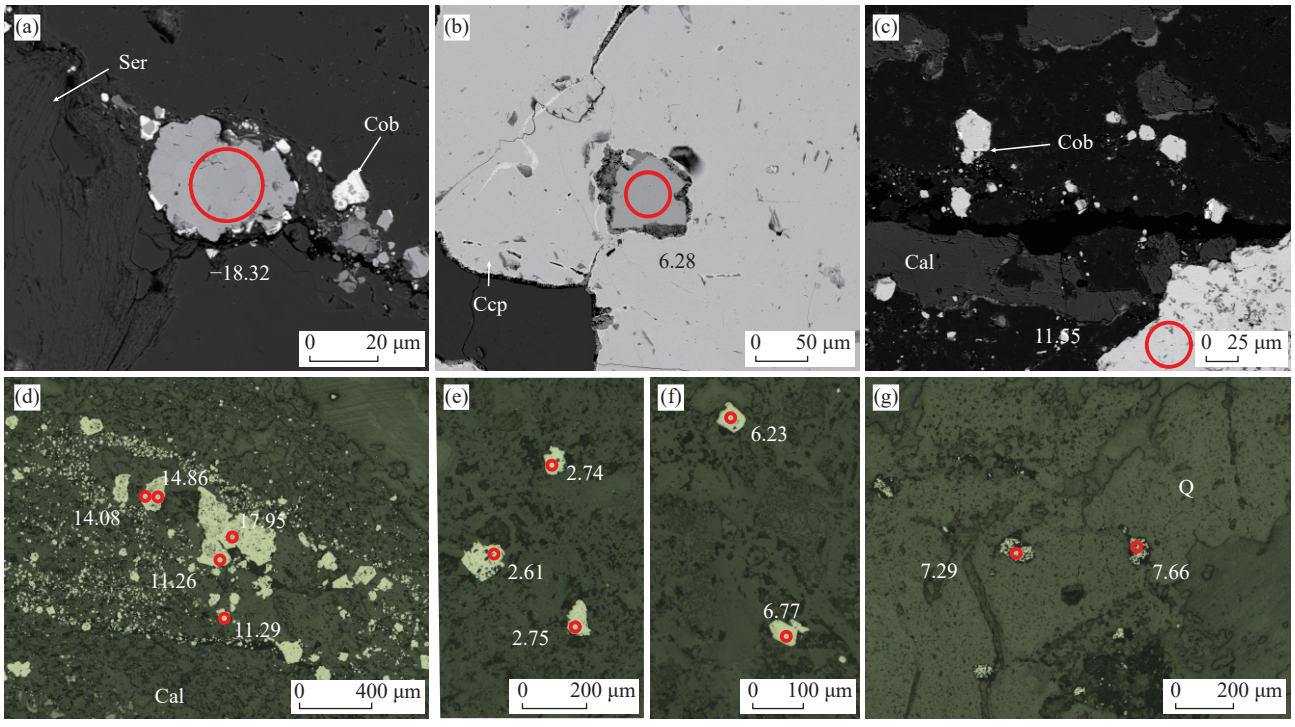


Fig. 10. BSE images (a–c) and photomicrographs (d–g) showing $\delta^{34}S$ values of pyrite. a–Pyrite of pre-mineralization stage in slate; b–pyrite in Cu mineralization stage enveloped by chalcopyrite; c–pyrite in Co mineralization stage; d–pyrite of pre-mineralization stage in limestone shows a core-rims texture, with the Co mineralization stage pyrite in rim; e, f–pyrite in two mafic dikes; g–Cu mineralization stage pyrite in quartz veins. Ser–sericite; Cob–cobaltite; Ccp–chalcopyrite; Cal–calcite; Q–quartz.

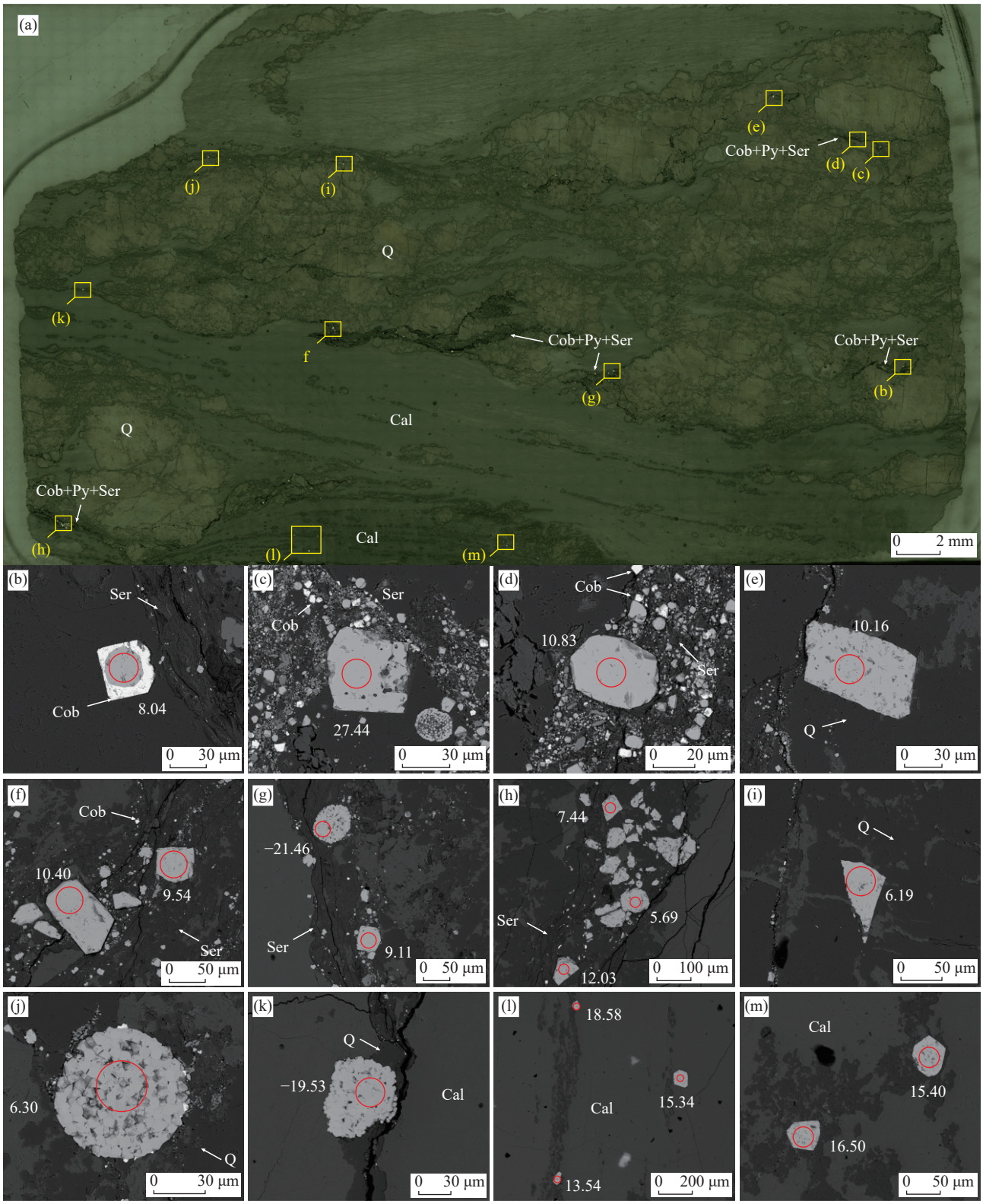


Fig. 11. BSE images showing $\delta^{34}S$ values of pyrite in structural breccia (a); b–d, f, h–pyrite in Co mineralization stage; e, i, j–pyrite in Cu mineralization stage; g, k–pyrite of pre-mineralization stage in slate breccia; l, m–pyrite of pre-mineralization stage in limestone breccia. Ser–sericite; Py–pyrite; Cob–cobaltite; Ccp–chalcopyrite; Cal–calcite; Q–quartz.

ZJ et al., 2021). Due to these two processes, sedimentary rocks in the continental crust are potential sources of Co metal.

Previous research has shown that the metamorphic basement of the West Qinling Orogen contains significant amounts of mate-mafic rocks with elevated cobalt concentrations (Holzheid A et al., 1996; Zhang HF et al., 2007a; Su BX et al., 2023). Cobalt primarily occurs in olivine and pyroxene and exhibits chalcophile characteristics, with partition coefficients between sulfide and silicate melts

Table 3. *In situ* Sr isotope Data of the Xiji Cu-Co deposit.

Sample	Description	$^{87}Sr/^{86}Sr$	2SE	$^{84}Sr/^{86}Sr$	2SE	$^{88}Sr(V)$	$^{85}Rb(V)$	Rb/Sr
HHQ-01	Cal4	0.709655	0.000070	0.0564	0.0001	4.22	0.00	0.0000120214
HHQ-02	Cal4	0.709943	0.000135	0.0576	0.0002	1.58	0.00	0.0000275045
HHQ-03	Cal4	0.709834	0.000151	0.0573	0.0001	1.68	0.00	0.0000014271
HHQ-04	Cal4	0.711242	0.000111	0.0568	0.0001	1.66	0.00	0.0000243326
HHQ-05	Cal4	0.711232	0.000170	0.0572	0.0002	1.49	0.00	0.0000152420
HHQ-06	Cal4	0.710981	0.000115	0.0572	0.0001	1.43	0.00	0.0000145962
HHQ-07	Cal4	0.711368	0.000124	0.0569	0.0001	1.88	0.00	−0.0000008913
HHQ-08	Cal4	0.710436	0.000140	0.0569	0.0001	1.64	0.00	−0.0000058533
HHQ-09	Cal4	0.709987	0.000216	0.0573	0.0002	1.18	0.00	0.0000306130
HHQ-10	Cal4	0.709800	0.000160	0.0570	0.0001	1.53	0.00	0.0000149078
HHQ-11	Cal4	0.709627	0.000101	0.0563	0.0001	2.74	0.00	0.0000088356
HHQ-12	Cal4	0.709631	0.000087	0.0565	0.0001	2.62	0.00	0.0000135285
HHQ-13	Cal2	0.709639	0.000098	0.0565	0.0001	2.35	0.00	−0.0000105006
HHQ-14	Cal2	0.709478	0.000095	0.0565	0.0001	2.22	0.00	−0.0000019951
HHQ-15	Cal2	0.709727	0.000104	0.0567	0.0001	2.07	0.00	−0.0000021580
HHQ-16	Cal2	0.709637	0.000109	0.0567	0.0001	1.98	0.00	0.0000159408
HHQ-17	Cal2	0.709865	0.000163	0.0576	0.0001	1.27	0.00	−0.0000029069
HHQ-18	Cal2	0.709577	0.000161	0.0572	0.0001	1.36	0.00	0.0000179593
HHQ-19	Cal2	0.709579	0.000135	0.0570	0.0001	1.56	0.00	−0.0000017538
HHQ-20	Cal2	0.709706	0.000134	0.0571	0.0001	1.39	0.00	0.0000285378
HHQ-21	Cal2	0.709680	0.000105	0.0567	0.0001	2.09	0.00	−0.0000050611
HHQ-22	Cal2	0.709493	0.000255	0.0594	0.0003	0.67	0.00	−0.0000245526
HHQ-27	Cal1	0.710227	0.000245	0.0580	0.0002	0.94	0.00	0.0000240285
HHQ-28	Cal1	0.709764	0.000220	0.0575	0.0002	1.00	0.00	−0.0000076256
HHQ-29	Cal1	0.709983	0.000227	0.0577	0.0002	1.04	0.00	0.0000336444
HHQ-30	Cal1	0.709848	0.000264	0.0578	0.0002	0.84	0.00	0.0000292255
HHQ-31	Cal1	0.709664	0.000231	0.0580	0.0002	0.94	0.00	0.0000512216
HHQ-32	Cal1	0.709904	0.000248	0.0576	0.0002	1.13	0.00	0.0000144928
HHQ-33	Cal1	0.709693	0.000248	0.0582	0.0002	0.92	0.00	0.0000846711
HHQ-34	Cal3	0.709833	0.000213	0.0577	0.0002	1.18	0.00	0.0000222799
HHQ-35	Cal3	0.709799	0.000216	0.0576	0.0002	1.27	0.00	0.0000373985
HHQ-36	Cal3	0.709791	0.000165	0.0571	0.0002	1.55	0.00	0.0000332638
HHQ-37	Cal3	0.709347	0.000246	0.0570	0.0002	1.35	0.00	0.0002141881
HHQ-38	Cal3	0.710291	0.000252	0.0580	0.0002	1.03	0.00	0.0000221610
HHQ-39	Cal3	0.709633	0.000252	0.0575	0.0002	1.28	0.00	0.0000526719
HHQ-40	Cal3	0.709601	0.000123	0.0567	0.0001	2.61	0.00	0.0000002058

ranging from 20 to 580 (Klemme S et al., 2006; Patten C et al., 2013; Wang J et al., 2021). This geochemical behavior enables effective Co mobilization into hydrothermal fluids, confirming the metamorphic basement of the West Qinling Orogen as a substantial Co contributor to mineralization. Nevertheless, the $^{87}Sr/^{86}Sr$ ratio of Triassic granites derived from the melting of meta-mafic rocks in the metamorphic basement (Zhang HF et al., 2007a) is lower than that of ore-forming fluids (Fig. 13), indicating that the ascending ore-forming fluids had high compositional complexity due to the incorporation of external materials.

The pre-mineralization stage pyrite in the slate displayed notably higher concentrations of As, Se, and Mg along the altered rims, without any alteration in the Co content (Fig. 9), suggesting that the subsequent hydrothermal fluids were enriched in As, and the pyrite in the wall rock failed to provide Co. It has been confirmed that steady-state lattice diffusion caused by vacancies in the presence of fluid can promote the preferential release of Co metals into ore-forming fluids (Qiu ZJ et al., 2025). However, this mechanism requires a high cobalt content of pyrite (approximately 3%), which is considerably higher than the cobalt content in limestone and slate (about 0.1%; Fig. 7), indicating it is improbable that the Co originated from the pyrite in the wall rock.

In contrast, pyrites in the mafic dike M1 exhibited anomalously high Co concentrations (about 2.3%; Fig. 7), indicating their potential as a Co source. The $^{87}Sr/^{86}Sr$ ratio decreased and increased (Fig. 13), indicating that ore-forming fluids are characterized by a shift from more mafic to less mafic (Avila TD et al., 2022; Adiatma YD et al., 2024). Corresponding to this evolutionary trend, the $\delta^{34}S$ values exhibited a slight increase from the Cu mineralization stage (+5.41‰ to +10.16‰) to the Co mineralization stage (+5.69‰ to +12.03‰; Fig. 12). The pyrites from the two mafic dikes displayed different $\delta^{34}S$ values (Fig. 12). The $\delta^{34}S$ values in the Cu mineralization stage (+5.41‰ to +10.16‰) were more similar to those of the cobalt-enriched mafic dike

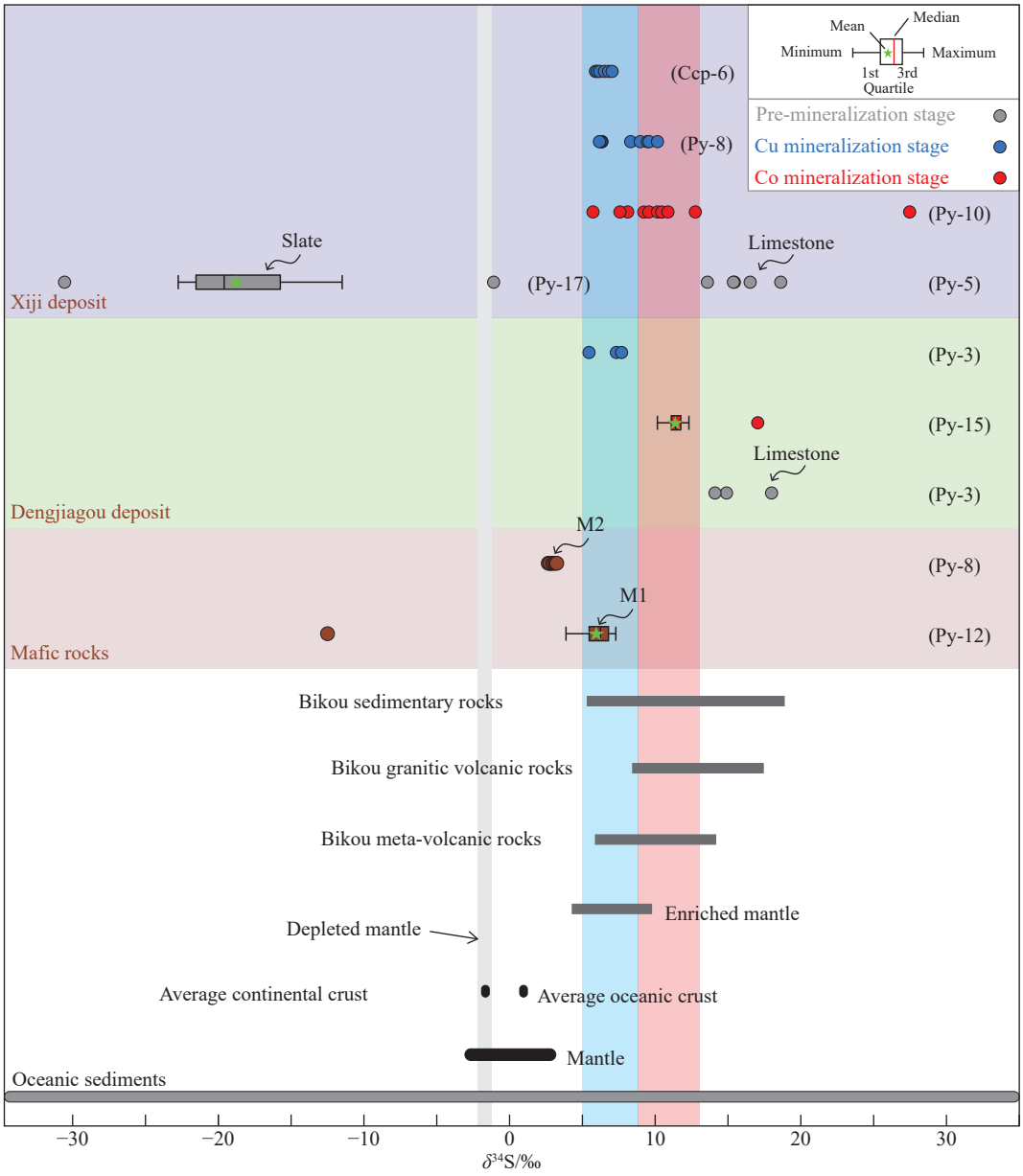


Fig. 12. $\delta^{34}S$ values ‘‘Box” plot of Xiji deposit, Dengjiagou deposit, and mafic rocks. Other $\delta^{34}S$ values data: Bikou sedimentary rocks, granitic volcanic rocks, and meta-volcanic rocks (Yue SW et al., 2013; Zhao HS et al., 2021); enriched mantle and depleted mantle (Labidi J et al., 2015); mantle (Ohmoto H, 1972); average oceanic crust and oceanic sediments (Rielli A et al., 2018).

M1 (+3.90‰ to +7.30‰; Fig. 12). The $\delta^{34}S$ values of mafic dike M2 ranged from +2.61‰ to +3.21‰, slightly lower than that of mafic dike M1 (+3.90‰ to +7.30‰) and consistent with mantle-derived sulfur (−3‰ to +3‰; Fig. 12; Ohmoto H, 1972). These pieces of evidence explain that ore-forming fluids interacted with mafic dike M1, with the reaction intensity diminishing during mineralization. This fluid-rock interaction resulted in higher $\delta^{34}S$ values in mafic dike M1 and lower $\delta^{34}S$ values in the initial Cu mineralization stage. During the reaction, the mafic dikes released Co metal into the ore-forming fluids through steady-state lattice diffusion (Qiu ZJ et al., 2025). Mafic dike M1 occurs at 20 m depth, closer to the orebody than mafic dike M2 (50 m depth), supporting this interpretation. These pieces of evidence imply that the mafic dikes did not supply the ore-forming fluids. Instead, they interacted with ore-forming fluids from the metamorphic basement, contributing Co metal to the hydrothermal system.

6.4. Genetic model of the Xiji Cu-Co deposit

In the northern segment of the West Qinling Orogen, Mn-Co and Cu-Co deposits hosted in Devonian greenschist-facies metasedimentary rocks (e.g., Dengjiagou, Shangtong, Lijiashan, Lujiagou; Fig. 1) are associated with EW-trending brittle-ductile shear zones, which are secondary or higher-order structures of regional thrusts. The $\delta^{34}S$ values of the Cu and Co mineralization stages in the Xiji deposit (range from +5.92‰ to +10.16‰ and from +5.69‰ to +12.03‰, respectively) coincide with the $\delta^{34}S$ values of the corresponding stage in the Dengjiagou deposit (range from +5.41‰ to +7.29‰ and from +10.11‰ to +12.30‰,

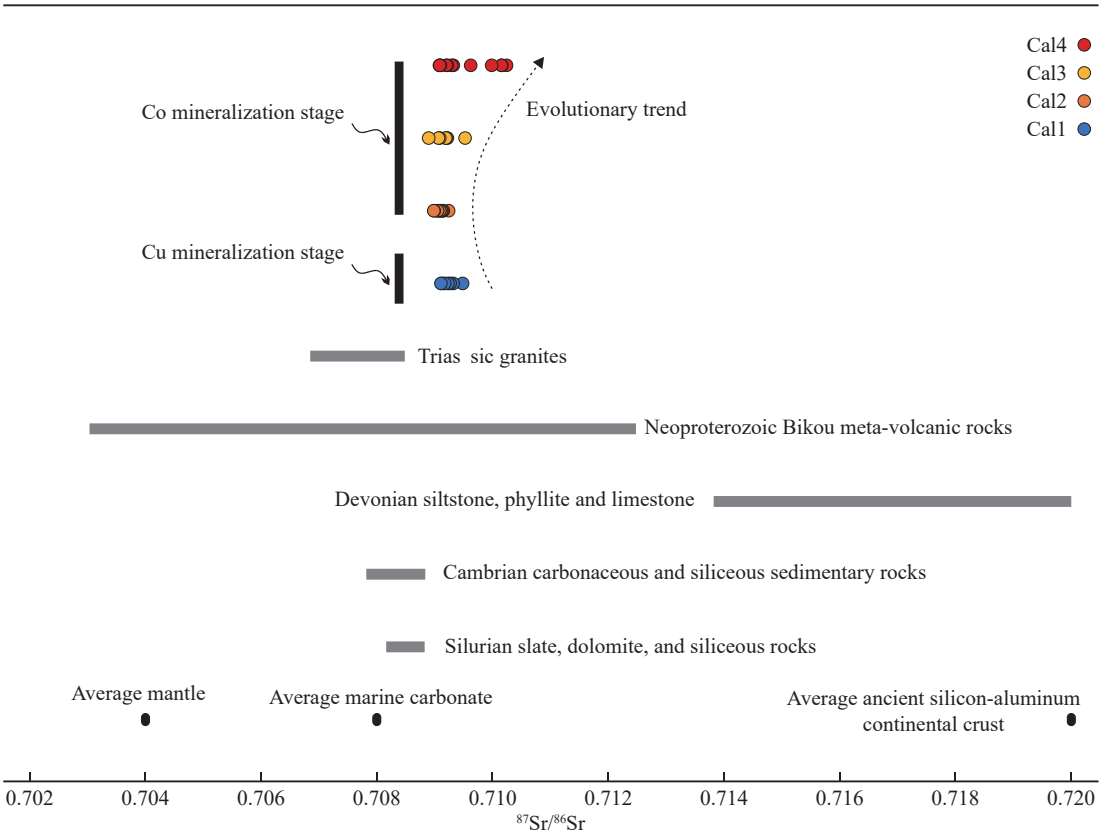


Fig. 13. $^{87}Sr/^{86}Sr$ plot of calcite in the Xiji deposit. Data sources are as follows: Triassic granites (Zhang HF et al., 2007a, b); Neoproterozoic Bikou meta-volcanic rocks (Xia LQ et al., 2007; He CG, 2022); Devonian siltstone, phyllite and limestone (Zhang L et al., 2009); Cambrian carbonaceous and siliceous sedimentary rocks and Silurian slate, dolomite, and siliceous rocks (Liu JJ et al., 2014); average mantle, marine carbonate, and ancient silicon-aluminum continental crust (Hu QQ, 2015; Yin G et al., 2009).

respectively), suggesting the two deposits share similar ore-forming fluids, and the Xiji Cu-Co deposit is regionally representative (Fig. 12).

Sustained N-S compressional stress in the Xiji Cu-Co deposit facilitated brittle-ductile shearing at the limestone-slate interfaces in the limbs of E-W trending folds, where a significant contrast existed. The more competent limestone was subjected to cataclastic brecciation, whereas the less competent slate underwent ductile deformation, creating large brittle-ductile shear zones that created favorable space for mineralization (Fig. 14). Ore-forming fluids from the Neoproterozoic metamorphic basement discharged from regional thrust faults, such as the crustal Hezuo-Lintan-Liangdang fault and the secondary fault. They were channeled by higher-order brittle-ductile shear zones and beneath the low-permeability seals of the Devonian slate and local limestone that cap the hydrothermal system, resulting in the dispersed reaction of fluids with existing mafic dikes in the Cu-Co mineralization stage (Fig. 14). This interpretation is supported by the spatial correlation between brittle-ductile shear zones and wall rock and the *in situ* S-Sr isotope evidence at Xiji. The calcite U-Pb ages in the Cu and Co mineralization stages in the Xiji Cu-Co deposit range from 128 Ma to 118 Ma (unpublished data), contemporaneous with the regional Daqiao gold deposit (130.8 ± 3.1 Ma to 127.2 ± 0.6 Ma; Wu YF et al., 2019b). This spatiotemporal correlation suggests that the ore-forming fluid was likely triggered by far-field effects associated with plate reorganization during Paleo-Pacific plate subduction beneath eastern Eurasia.

7. Conclusions

(i) The Xiji Cu-Co deposit is a rare hydrothermal Co deposit with cobaltite as the independent cobalt-bearing mineral. It is structurally governed by EW-trending brittle-ductile shear zones. Preliminary explorations have identified 2000 t of Cu with a grade of 1.59×10^{-2} and estimated 120 t of Co with a grade of 0.1×10^{-2}.

(ii) The chalcopyrite and pyrites in the Cu and Co mineralization stage had a narrow range of $\delta^{34}S$ values (+5.92‰ to +10.16‰ and +5.69‰ to +12.03‰, respectively), which differed significantly from those of the pyrites in limestone (+13.54‰ to +18.58‰), slate (−31.67‰ to −1.08‰), and mafic dikes (+2.61‰ to +3.21‰ and +3.90‰ to +7.30‰), but fall within the range of those in the Neoproterozoic Bikou Group. The calcite $^{87}Sr/^{86}Sr$ ratio in the Cu and Co mineralization stages ranged from 0.709347 to 0.711368, differing from that of the strontium reservoirs in the West Qinling Orogen, except for the Neoproterozoic Bikou meta-volcanic rocks. These pieces of evidence indicate that ore-forming fluids were derived from the Neoproterozoic metamorphic basement, analogous to the Neoproterozoic Bikou Group, which contains extensive meta-mafic rocks. The abundance of meta-mafic rocks in the Neoproterozoic

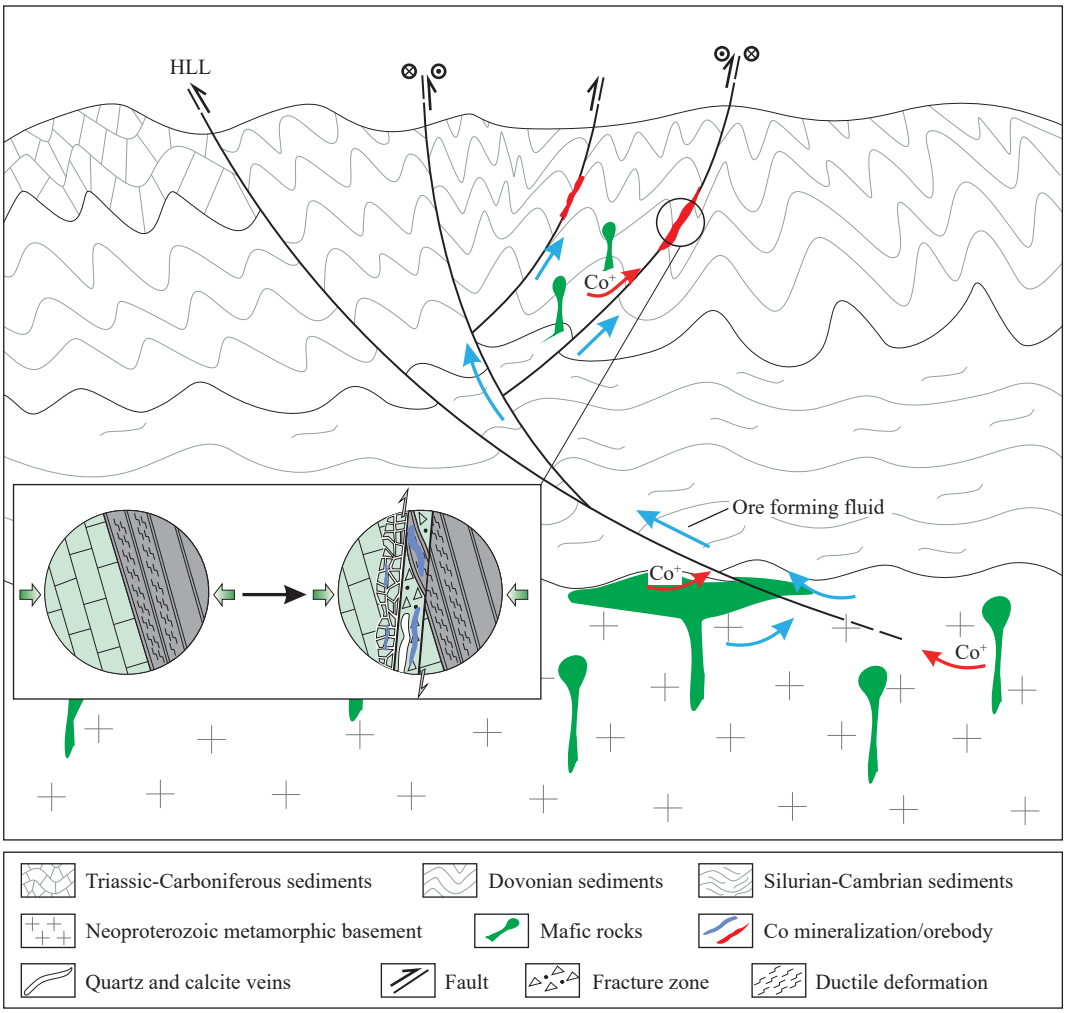


Fig. 14. Diagrammatic genetic model and structural deformation evolution of the Xiji Cu-Co deposit. HLL–Hezuo-Lintan-Liangdang fault.

metamorphic basement led to substantial cobalt enrichment in the derived ore-forming fluids. The trend of the $^{87}Sr/^{86}Sr$ ratio indicates a shift in the ore-forming fluid from more mafic to less mafic. The anomalously high Co concentrations of the pyrites in the mafic dikes and the inconsistency in the pyrite $\delta^{34}S$ values of the two mafic dikes suggest that the existing mafic dike reacted with the ore-forming fluids, releasing Co metal.

(iii) The similarity in the mineralization characteristics and the $\delta^{34}S$ values across the mineralization stages between the Dengjiagou and Xiji deposits indicate a regionally extensive hydrothermal Co mineralization event, demonstrating significant Co exploration potential in the West Qinling Orogen.

CRediT authorship contribution statement

Pan-Fei Sun, Yong-Sheng Li and Hai-Rui Sun conceived of the presented idea. Pan-Fei Sun and Zhao Liu carried out the experiment. All authors discussed the results and contributed to the final manuscript.

Declaration of competing interest

The authors declare no conflicts of interest.

Acknowledgments

This research was jointly supported by the Special Project on the Investigation of Basic Resources of Science and Technology (2022FY101701), the project of the China Geological Survey (DD20230203902), and the Science and Technology Support Program of the Ministry of Natural Resources of the People's Republic of China (ZKKJ202414).

References

Adiatma YD, Saltzman MR, Liu XM, Wang XK, Edwards CT. 2024. Lithium isotope stratigraphy and Ordovician weathering. Earth and Planetary Science Letters, 647, 119030. doi: 10.1016/j.epsl.2024.119030.

Avila TD, Saltzman MR, Adiatma YD, Joachimski MM, Griffith EM, Olesik JW. 2022. Role of seafloor production versus continental basalt weathering in Middle to Late Ordovician seawater $^{87}Sr/^{86}Sr$ and climate. Earth and Planetary Science Letters, 593, 117641. doi: 10.1016/j.epsl.2022.117641.

Bending JS, Scales WG. 2001. New production in the Idaho cobalt belt: A unique metallogenic province. Applied Earth Science, 110(2), 81–87. doi: 10.1179/aes.2001.110.2.81.

Berglund M, Wieser ME. 2010. Isotopic compositions of the elements 2009 (IUPAC technical report). Pure and Applied Chemistry, 83(2), 397–410. doi: 10.1351/pac-rep-10-06-02.

Brown AC. 2014. Low-temperature sediment-hosted copper deposits. Treatise on Geochemistry. Amsterdam: Elsevier, 251–271. doi: 10.1016/b978-0-08-095975-7.01110-4.

Cailteux JLH, Kampunzu AB, Lerouge C, Kaputo AK, Milesi JP. 2005. Genesis of sediment-hosted stratiform copper–cobalt deposits, central African Copperbelt. Journal of African Earth Sciences, 42(1-5), 134–158. doi: 10.1016/j.jafrearsci.2005.08.001.

Cao GS, Zhang Y, Chen HY. 2023. Trace elements in pyrite from orogenic gold deposits: Implications for metallogenic mechanism. Acta Petrologica Sinica, 39(8), 2330–2346 (in Chinese with English abstract). doi: 10.18654/1000-0569/2023.08.06.

Chen YJ, Santosh M. 2014. Triassic tectonics and mineral systems in the Qinling Orogen, Central China. Geological Journal, 49(4–5), 338–358. doi: 10.1002/gj.2618.

Ding XJ, Qian LR, Jiang WL, Liu HL, Yiming A, Zha M, Qu JX, Jiang ZF. 2024. Review of bacterial sulfate reduction in lacustrine deposition and its identification in the Jimsar Sag, Junggar Basin. Marine and Petroleum Geology, 163, 106801. doi: 10.1016/j.marpetgeo.2024.106801.

Dong YP, Santosh M. 2016. Tectonic architecture and multiple orogeny of the Qinling Orogenic Belt, Central China. Gondwana Research, 29(1), 1–40. doi: 10.1016/j.gr.2015.06.009.

Dong YP, Zhang GW, Hauzenberger C, Neubauer F, Yang Z, Liu XM. 2011. Palaeozoic tectonics and evolutionary history of the Qinling orogen: Evidence from geochemistry and geochronology of ophiolite and related volcanic rocks. Lithos, 122(1–2), 39–56. doi: 10.1016/j.lithos.2010.11.011.

Dong YP, Zhang GW, Neubauer F, Liu XM, Genser J, Hauzenberger C. 2011. Tectonic evolution of the Qinling Orogen, China: Review and synthesis. Journal of Asian Earth Sciences, 41(3), 213–237. doi: 10.1016/j.jseaes.2011.03.002.

DRCCGS (Development and Research Center, China Geological Survey). 2023. Research report on the investigation, evaluation and prospecting prediction of cobalt resources in the Xiji deposit, Gansu Province (in Chinese).

Duan XP, Meng FC, Wang ZQ, Yu XF. 2024. Metallogenic characteristics of Shitoukengde intrusion and its implications for Ni-Co-(Cu) sulfide mineralization in East Kunlun. China Geology, 7(4), 714–729. doi: 10.31035/cg2023070.

El Desouky HA, Muchez P, Cailteux J. 2009. Two Cu–Co sulfide phases and contrasting fluid systems in the Katanga Copperbelt, Democratic Republic of Congo. Ore Geology Reviews, 36(4), 315–332. doi: 10.1016/j.oregeorev.2009.07.003.

Feng YM, Cao XD, Zhang EP, Hu YX, Pan XP, Yang JL, Jia QZ, Li WM. 2003. Tectonic evolution framework and nature of the west Qinling orogenic belt. Northwestern Geology, 36(1), 1–10 (in Chinese with English abstract).

Guo MX, Liu JJ, Zhai DG, Weng GM, Zhu R. 2024. Discovery of scheelite in the Zaozigou gold deposit of West Qinling Orogen, Northwest China and its implications for ore genesis. China Geology, 7(3), 586–588. doi: 10.31035/cg2023099.

He CG. 2022. Geology, Mineralization, and Genesis of Typical Gold Deposits in The Northern Belt of The West Qinling Orogen. Wuhan, China University of Geosciences, Ph. D thesis, 1–187 (in Chinese with English abstract). doi: 10.27492/d.cnki.gzdzu.2022.000029.

Holzheid A, Borisov A, Palme H. 1994. The effect of oxygen fugacity and temperature on solubilities of nickel, cobalt, and molybdenum in silicate melts. Geochimica et Cosmochimica Acta, 58(8), 1975–1981. doi: 10.1016/0016-7037(94)90429-4.

Hu QQ. 2015. The Mineralization Features, Mechanism and Metallogenic Regularity of The Fengtai Pb-Zn Polymetallie Ore Cluster in West Qinling, China. Beijing, Chinese Academy of Geological Sciences, Ph. D thesis, 1–133 (in Chinese with English abstract).

Hu ZC, Zhang W, Liu YS, Gao S, Li M, Zong KQ, Chen HH, Hu SH. 2015. “Wave” signal-smoothing and mercury-removing device for laser ablation quadrupole and multiple collector ICPMS analysis: Application to lead isotope analysis. Analytical Chemistry, 87(2), 1152–1157. doi: 10.1021/ac503749k.

Johnson CA, Bookstrom AA, Slack JF. 2012. Sulfur, carbon, hydrogen, and oxygen isotope geochemistry of the Idaho cobalt belt. Economic Geology, 107(6), 1207–1221. doi: 10.2113/econgeo.107.6.1207.

Klemme S, Günther D, Hametner K, Prowatke S, Zack T. 2006. The partitioning of trace elements between ilmenite, ulvospinel, armalcolite and silicate melts with implications for the early differentiation of the Moon. Chemical Geology, 234(3–4), 251–263. doi: 10.1016/j.chemgeo.2006.05.005.

Kontak DJ, Kerrich R. 1995. Geological and geochemical studies of a metaturbidite-hosted lode gold deposit; the Beaver Dam Deposit, Nova Scotia; II, Isotopic studies. Economic Geology, 90(4), 885–901. doi: 10.2113/gsecongeo.90.4.885.

Kontak DJ, Kerrich R. 1997. An isotopic (C, O, Sr) study of vein gold deposits in the Meguma Terrane, Nova Scotia; implication for source reservoirs. Economic Geology, 92(2), 161–180. doi: 10.2113/gsecongeo.92.2.161.

Labidi J, Cartigny P, Jackson MG. 2015. Multiple sulfur isotope composition of oxidized Samoan melts and the implications of a sulfur isotope ‘mantle array’ in chemical geodynamics. Earth and Planetary Science Letters, 417, 28–39. doi: 10.1016/j.epsl.2015.02.004.

Large RR, Mukherjee I, Gregory D, Steadman J, Corkrey R, Danyushevsky LV. 2019. Atmosphere oxygen cycling through the Proterozoic and Phanerozoic. Mineralium Deposita, 54(4), 485–506. doi: 10.1007/s00126-019-00873-9.

Liu JJ, Liu CH, Carranza EJM, Li YJ, Mao ZH, Wang JP, Wang YH, Zhang J, Zhai DG, Zhang HF, Shan L, Zhu LM, Lu RK. 2015. Geological characteristics and ore-forming process of the gold deposits in the western Qinling region, China. Journal of Asian Earth Sciences, 103, 40–69. doi: 10.1016/j.jseaes.2014.11.012.

Liu WH, Borg SJ, Testemale D, Etschmann B, Hazemann JL, Brugger J. 2011. Speciation and thermodynamic properties for cobalt chloride complexes in hydrothermal fluids at 35–440°C and 600bar: An *in situ* XAS study. Geochimica et Cosmochimica Acta, 75(5), 1227–1248. doi: 10.1016/j.gca.2010.12.002.

Lu YG, Hao B, Sun K, He SF, Xu KK, Gong PH, Zhang H. 2020. General situation of cobalt resource and its utilization analysis. Geological Survey and Research, 43(1), 72–80 (in Chinese with English abstract).

Mao JW, Qiu YM, Goldfarb RJ, Zhang ZC, Garwin S, Ren FS. 2002. Geology, distribution, and classification of gold deposits in the western Qinling belt, Central China. Mineralium Deposita, 37(3), 352–377. doi: 10.1007/s00126-001-0249-0.

Mattauer M, Matte P, Malavieille J, Tapponnier P, Maluski H, Qin XZ, Lun LY, Qin TY. 1985. Tectonics of the Qinling Belt: Build-up and evolution of eastern Asia. Nature, 317(6037), 496–500. doi: 10.1038/317496a0.

McGowan RR, Roberts S, Boyce AJ. 2006. Origin of the Nchanga copper–cobalt deposits of the Zambian Copperbelt. Mineralium Deposita, 40(6), 617–638. doi: 10.1007/s00126-005-0032-8.

Meng QR, Zhang GW. 1999. Timing of collision of the north and South China blocks: Controversy and reconciliation. Geology, 27(2), 123. doi: 10.1130/0091-7613(1999)027<0123:tocotn>2.3.co;2.

Patten C, Barnes SJ, Mathez EA, Jenner FE. 2013. Partition coefficients of chalcophile elements between sulfide and silicate melts and the early crystallization history of sulfide liquid: LA-ICP-MS analysis of MORB sulfide droplets. Chemical Geology, 358, 170–188. doi: 10.1016/j.chemgeo.2013.08.040.

Ohmoto H. 1972. Systematics of sulfur and carbon isotopes in

hydrothermal ore deposits. Economic Geology, 67(5), 551–578. doi: 10.2113/gsecongeo.67.5.551.

Qiu KF, Yu HC, Gou ZY, Liang ZL, Zhang JL, Zhu R. 2018. Nature and origin of Triassic igneous activity in the western Qinling Orogen: The Wenquan composite pluton example. International Geology Review, 60(2), 242–266. doi: 10.1080/00206814.2017.1334598.

Qiu ZJ, Fan HR, Goldfarb R, Tomkins AG, Yang KF, Li XC, Xie LW, Liu X. 2021. Cobalt concentration in a sulfidic sea and mobilization during orogenesis: Implications for targeting epigenetic sediment-hosted Cu-Co deposits. Geochimica et Cosmochimica Acta, 305, 1–18. doi: 10.1016/j.gca.2021.05.001.

Qiu ZJ, Xing YL, Brugger J, Etschmann B, Pintér Z, Fougerouse D, Xu J, Yu ZY, Guo GJ, Fan HR. 2025. Vacancies in sulfides facilitate fluid-induced solid-state diffusion and critical metals accumulation. Nature Communications, 16, 1835. doi: 10.1038/s41467-025-57171-4.

Ren JS. 1996. The continental tectonics of China. Journal of Southeast Asian Earth Sciences, 13(3–5), 197–204. doi: 10.1016/0743-9547(96)00026-8.

Rielli A, Tomkins AG, Nebel O, Raveggi M, Jeon H, Martin L, Ávila JN. 2018. Sulfur isotope and PGE systematics of metasomatised mantle wedge. Earth and Planetary Science Letters, 497, 181–192. doi: 10.1016/j.epsl.2018.06.012.

Saintilan NJ, Selby D, Creaser RA, Dewaele S. 2018. Sulphide re-Os geochronology links orogenesis, salt and Cu-Co ores in the Central African Copperbelt. Scientific Reports, 8, 14946. doi: 10.1038/s41598-018-33399-7.

Sillitoe RH, Perelló J, Creaser RA, Wilton J, Dawborn T. 2015. Two ages of copper mineralization in the mWombezhi dome, northwestern Zambia: Metallogenic implications for the central African copperbelt. Economic Geology, 110(8), 1917–1923. doi: 10.2113/econgeo.110.8.1917.

Sillitoe RH, Perelló J, Creaser RA, Wilton J, Wilson AJ, Dawborn T. 2017. Age of the Zambian copperbelt. Mineralium Deposita, 52(8), 1245–1268. doi: 10.1007/s00126-017-0726-8.

Slack JF, Causey JD, Eppinger RG, Gray JE, Johnson CA, Lund KI, Schulz KJ. 2010. Co-Cu-Au deposits in metasedimentary rocks: A preliminary report. US Geological Survey Open-File Report 2010–1212, US Geological Survey.

Sośnicka M, Gigler GM, Kinnaird JA, Przybyłowicz WJ, Chimvinga J, Master S, Plessen B. 2019. Mineralizing fluids of the supergene-enriched Mashitu south Cu-co deposit, Katanga copperbelt, DRC. Ore Geology Reviews, 109, 201–228. doi: 10.1016/j.oregeorev.2019.04.001.

Su BX, Qin KZ, Jiang SY, Cao MJ, Zhang ZC, Zhang HL, Xue GQ, Zhou TF, Mo JP. 2023. Mineralization regularity, scientific issues, prospecting technology and research prospect of Co-Ni deposits in China. Acta Petrologica Sinica, 39(4), 968–980 (in Chinese with English abstract). doi: 10.18654/1000.0569/2023.04.02.

Sun PF, Wang QF, Li HJ, Dong CY, Deng J. 2020. Geology and pyrite sulfur isotopes of the Suoluogou gold deposit: Implication for crustal continuum model of orogenic gold deposit in northwestern margin of Yangtze Craton, SW China. Ore Geology Reviews, 122, 103487. doi: 10.1016/j.oregeorev.2020.103487.

Tian F, Wang KY, Liang YH, Li SD, Dong GH. 2017. Characteristies of hydrothermal superimposed mineralization and source of ore-forming fluids in the Dahenglu Co-Cu Deposit. Northwestern Geology, 50(2), 167–177 (in Chinese with English abstract). doi: 10.19751/j.cnki.61-1149/p.2017.02.018.

Tong XR, Liu YS, Hu ZC, Chen HH, Zhou L, Hu QH, Xu R, Deng LX, Chen CF, Yang L, Gao S. 2016. Accurate determination of Sr isotopic compositions in clinopyroxene and silicate glasses by LA-MC-ICP-MS. Geostandards and Geoanalytical Research, 40(1), 85–99. doi: 10.1111/j.1751-908X.2015.00315.x.

Van Wilderode J, Debruyne D, Torremans K, Elburg MA, Vanhaecke F, Muchez P. 2015. Metal sources for the nkana and konkola stratiform Cu–co deposits (Zambian copperbelt): Insights from Sr and Nd isotope ratios. Ore Geology Reviews, 67, 127–138. doi: 10.1016/j.oregeorev.2014.11.011.

Wafik A, Zoheir B, Benchekroun F, Benaouda R, Ben Massoude M, Atif Y, Pour AB, Niroomand S, El Arbaoui A, Karfal A, Maacha L. 2024. Multistage gold-polymetallic mineralization in the bou azzer district, anti-atlas, Morocco: Insights from ore microscopic, geochemical, and fluid inclusion studies. Geofluids, 2024, 5579902. doi: 10.1155/2024/5579902.

Wang HN, Liu FL, Zhu ZY, Wang F, Tian ZH. 2023. Complex evolution of the sedimentation, metamorphism-deformation and hydrothermal processes and their constrains on the occurrence, enrichment and mineralization of Co in the Dahenglu Cu-Co deposit Jilin Province. Acta Petrologica Sinica, 39(4), 998–1018 (in Chinese with English abstract). doi: 10.18654/1000-0569/2023.04.04.

Wang J, Su BX, Robinson PT, Xiao Y, Bai Y, Liu X, Sakyi PA, Jing JJ, Chen C, Liang Z, Bao ZA. 2021. Trace elements in olivine: Proxies for petrogenesis, mineralization and discrimination of mafic-ultramafic rocks. Lithos, 388–389, 106085. doi: 10.1016/j.lithos.2021.106085.

Wang XS, Bi XW, Hu RZ, Leng CB, Yin GH, Yu HJ. 2015. S-Pb isotopic geo-chemistry of Xiuwacu magmatic hydrothermal Mo-W deposit in Zhongdian area, NW Yunnan: constrains on the sources of metal. Acta Petrologica Sinica, 31(11), 3171–3188 (in Chinese with English abstract).

Wang Y, Guo CH, Du C, Chen XJ, Jia LQ, Guo XN, Chen RS, Zhang MS, Chen ZY, Wang HD,. 2021. Carbon peak and carbon neutrality in China: Goals, implementation path, and prospects. China Geology, 4, 1–27. doi: 10.31035/cg2021083.

Wang Y, Shi YH, Chen BL, Tan RW, Gao Y, Shen JH. 2019. Zircon U-Pb age of Fengxian acid pyroclastic rocks and its enlightenment to the existence of Pan-African orogeny in the West Qinling Orogenic Belt, China. China Geology, 3(4), 1–3. doi: 10.31035/cg2018130.

Wu GL, Meng QR, Duan L, Li L. 2014. Early Mesozoic structural evolution of the eastern West Qinling, northwest China. Tectonophysics, 630, 9–20. doi: 10.1016/j.tecto.2014.05.008.

Xia LQ, Xia ZH, Xu XY, Li XM, Ma ZP. 2007. Petrogenesis of the Bikou Group volcanic rocks. Earth Science Frontiers, 14(3), 084–101 (in Chinese with English abstract).

Yan Z, Aitchison JC, Fu CL, Guo XQ, Xia WJ, Niu ML. 2016. Devonian sedimentation in the xiqingshan mountains: Implications for paleogeographic reconstructions of the SW Qinling Orogen. Sedimentary Geology, 343, 1–17. doi: 10.1016/j.sedgeo.2016.07.009.

Yin G, Ni SJ, Shi ZM, Gao ZY, Huang Y, Yan QS. 2009. Isotope Geochemistry. Beijing, Geological Publishing House, 1–407 (in Chinese).

Yue SW, Lin ZW, Deng XH, Li FR, He HX, Feng AG. 2013. C, H, O, S, Pb isotopic geochemistry of the Jianchaling gold deposit, Shaanxi Province. Geotectonica et Metallogenia, 37(4), 653–670 (in Chinese with English abstract). doi: 10.16539/j.ddgzyckx.2013.04.006.

Zeng QT, McCuaig TC, Tohver E, Bagas L, Lu YJ. 2014. Episodic Triassic magmatism in the western South Qinling Orogen, Central China, and its implications. Geological Journal, 49(4-5), 402–423. doi: 10.1002/gj.2571.

Zhang GW, Meng QR, Lai SC. 1995. Tectonics and structure of Qinling orogenic belt. Science in China (Series B), 38(11), 1379–1394.

Zhang GW, Zhang BR, Yuan XC, Xiao QH. 2001. The Qinling Orogen and Continental Dynamics. Beijing, China Scientific and Technical Publishers, 1–863 (in Chinese).

Zhang HR, Hou ZQ, Yang ZM, Song YC, Liu YC, Chai P. 2020. A new division of genetic types of cobalt deposits: Implications for Tethyan cobalt-rich belt. Mineral Deposits, 39(3), 501–510 (in Chinese with English abstract). doi: 10.16111/j.0258-7106.2020.03.007.

Zhang L, Yang RS, Mao SD, Lu YH, Qin Y, Liu HJ. 2009. Sr and Pb isotopic feature and ore-forming material source of the Yangshan gold deposit. Acta Petrologica Sinica, 25(11), 2811–2822 (in Chinese with English abstract).

Zhang LC, Zhang AK, Liu YL, Li W, Dong ZG, Gao BY, Wang CL, Zhu MT. 2023. Reserch progresses and problems of sedimentary-metasedimentary rock-hosted cobalt deposits. Acta petrologica Sinica, 39(4), 981–997 (in Chinese with English abstract). doi: 10.18654/1000-0569/2023.04.03.

Zhang W, Hu ZC, Liu YS. 2020. Iso-Compass: New freeware software for isotopic data reduction of LA-MC-ICP-MS. Journal of Analytical Atomic Spectrometry, 35(6), 1087–1096. doi: 10.1039/d0ja00084a.

Zhang W, Hu ZC, Liu YS, Wu T, Deng XD, Guo JL, Zhao H. 2018. Improved *in situ* Sr isotopic analysis by a 257 nm femtosecond laser in combination with the addition of nitrogen for geological minerals. Chemical Geology, 479, 10–21. doi: 10.1016/j.chemgeo.2017.12.018.

Zhang ZP, Wu YF, Li JW. 2018. Characteristics and genesis of the silicified breccias in the Daqiao gold deposit, West Qinling Orogen. Geological Science and Technology Information, 37(2), 79–88 (in Chinese with English abstract). doi: 10.19509/j.cnki.dzkq.2018.0211.

Zhao HS, Wang QF, Groves DI, Deng J. 2021. Progressive spatial and temporal evolution of tectonic triggers and metasomatized mantle lithosphere sources for orogenic gold mineralization in a Triassic convergent margin: Kunlun-Qinling Orogen, Central China. GSA Bulletin, 133(11-12), 2378–2392. doi: 10.1130/b35754.1.

Zhao JX, Li GM, Qin KZ, Tang DM. 2019. A review of the types and ore mechanism of the cobalt deposits. Chinese Science Bulletin, 64(24), 2484–2500 (in Chinese with English abstract). doi: 10.1360/N972019-00134.